

TIME AVERAGE NEUTRALIZED MIGMA: A COLLIDING BEAM/PLASMA HYBRID PHYSICAL STATE AS ANEUTRONIC ENERGY SOURCE – A REVIEW

Bogdan C. MAGLICH

Aneutronic Energy Laboratory, United Sciences, Inc., P.O. Box 3037, Princeton, NJ 08543, USA

A D^+ beam of kinetic energy $T_i = 0.7$ MeV was stored in a “simple mirror” magnetic field as self-colliding orbits or migma and neutralized by ambient, oscillating electrons whose bounce frequencies were externally controlled. Space charge density was exceeded by an order of magnitude without instabilities. Three nondestructive diagnostic methods allowed measurements of ion orbit distributions, ion storage times, ion energy distributions, nuclear reaction rate, and reaction product spectrum. Migma formed a disc 20 cm in diameter and 0.5 cm thick. Its ion density was sharply peaked in the center; the ion-to-electron temperature ratio was $T_i/T_e \sim 10^3$; ion-electron temperature equilibrium was never reached. The volume average and central D^+ density were $n = 3.2 \times 10^9 \text{ cm}^{-3}$ and $n_c = 3 \times 10^{10} \text{ cm}^{-3}$ respectively, compared to the space charge limit density $n_{sc} = 4 \times 10^8 \text{ cm}^{-3}$. The energy confinement time was $\tau_e = 20\text{--}30$ s, limited by the charge exchange reactions with the residual gas in the vacuum (5×10^{-9} Torr). The ion energy loss rate was 1.4 keV/s. None of the instabilities that were observed in mirrors at several orders of magnitude lower density occurred. The proton energy spectrum for $d+d \rightarrow T+p+4$ MeV shows that dd collided at an average crossing angle of 160° . Evidence for exponential density buildup has also been observed. Relative to Migma III results and measured in terms of the product of ion energy E , density n , and confinement time τ , device performance was improved by a factor of 500. Using the central fast ion density, we obtained the triple product: $Tn\tau \approx 4 \times 10^{14} \text{ keV s cm}^{-3}$, which is greater than that of the best fusion devices. The luminosity (collision rate per unit cross section) was $\sim 10^{29} \text{ cm}^{-2} \text{ s}^{-1}$, with 0.7 A ion current through the migma center.

The stabilizing features of migma are: (1) large Larmor radius; (2) small canonical angular momentum; (3) short axial length z (disc shape); (4) nonadiabatic motions in r and z ; (5) precession and energy spread; (6) ambipolar potential; (7) radial density gradient; (8) large ion-to-electron temperature ratio; (9) metal walls in z ; (10) suitability for external stabilization techniques (small volume, recurrent surfacing of ions); and particularly (11) diamagnetic well.

Extrapolation of the results to reactor densities led to a $D+^3He$ reactor “basic migma disc” 0.5 m in diameter and 0.25 m thick, suspended in a 10 T field, generating 1.5 MW(th). A 2-MW(e) power plant would consist of 3 such discs in a common volume, referred to as a triplet migmacell. Its specific power is projected to be 1 MW(e)/ton. A large power plant of any size would consist of a large number of migma discs in a common volume. The advantages of such modular systems are: (1) economy of mass production: capital cost per kW will be 25% that of fission and 10% that of DT fusion; (2) plants will be economical for all sizes above 10 kW(e); (3) minimal heat pollution, thanks to direct conversion of the charged ion kinetic energy into electricity; (4) no proliferative potential; and (5) large power-to-weight ratio due to absence of shielding. Anticipated physics problems in density increase are discussed.

1. Properties of the hybrid state

The Migma IV experiment [1] gave rise to an unusual state of ionized matter. From the point of view of a particle beam physicist, it is a stored hadron beam with a density far in excess of the space charge limit, time average neutralized by oscillating electrons. Seen by a plasma physicist, it is a non-Maxwellian, nonequilibrated “synthetic” plasma whose ion and electron motions are ordered and decoupled. The neutralized migma has features of both colliding beams and plasma, yet it does not satisfy the definition of either state.

The experiment demonstrated that the density of a ~ 1 -MeV ion beam, stored as self-colliding orbits or migma (fig. 1b), can exceed the space charge limit without instabilities if ambient electrons are made to oscillate through the migma at a bounce frequency higher than the ion cyclotron frequency; the frequency

was adjusted by the application of an external dc electric field. The energy lifetime of the neutralized beam was $\tau = 20\text{--}40$ s; it was limited only by the classical processes: charge exchange and Coulomb scattering with the residual gas in vacuum. Lifetime did not seem to be affected by the presence of the oscillating electrons. Although the confining magnetic field was of the simple mirror type, the negative-mass instability [2,3], $m=1$ flute instability [4–6], and ion-cyclotron [7] and Harris [2] instabilities, found in other mirror devices at several orders of magnitude lower ion density, did not occur.

If the observed τ is scaled up to Intersecting Storage Ring conditions using the known dependence on ion energy T_i , kinematic factor γ , and vacuum pressure p , $\tau \propto T_i^{3/2}/(p\gamma_i)$, we get $\tau > 10^8$ s, which is of the order of magnitude of the observed lifetime in the ISR. The maximum volume average ion number density n achieved in the colliding (central) region of migma was

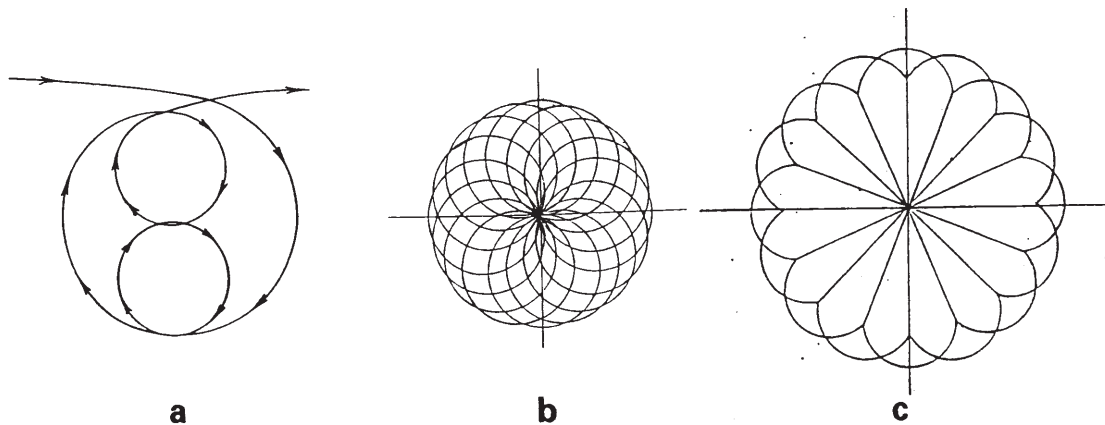


Fig. 1. Self-colliding beam (a), self-colliding orbits or magma (b), and diamagnetic magma (c). (a) The beam injected from the left into a magnetic field given by eq. (4) is made to collide head-on with itself at two intersecting points P. As time progresses, the figure of eight pattern rotates counterclockwise around P; the precession results in a self-colliding orbit mixture or "magma" pattern shown in (b). As the density of magma ions increases by continuous injection, one obtains a very large number of figure of eight orbits, the orbit density being sharply peaked in the center according to eq. (2). (c) The ion orbits, being electrically charged, generate a diamagnetic field that opposes the original field and cancels it everywhere except at the periphery (where the magma density is lowest); thus the colliding orbits become straight lines, equivalent to an infinite number of colliding beams intersecting through all crossing angles 0° – 180° . Nevertheless, due to the collision probability being proportional to σv_{12} , the weighted averaged crossing angle is 160° (see fig. 7).

limited solely by the injection current. It was $n = 3.2 \times 10^9 \text{ cm}^{-3}$, which is two orders of magnitude greater than that in the intersecting region of the ISR. If scaled up to ISR energy using the space charge limit dependence $n \propto T^{1/2}/\gamma$, the equivalent ISR ion density ion current would be 10^{12} cm^{-3} , i.e., two orders of magnitude higher than that in the ISRs; this would correspond to a coasting ion current of 1000 A. The magma luminosity is given now in terms of the average particle

number density n (cm^{-3}), relative velocity β_{12} , and magma volume V :

$$L = \int_V^{1/2} \beta_{12} c n^2 dV \approx \frac{1}{2} \beta_{12} c n^2 V. \quad (1)$$

We observed $L \sim 10^{29} \text{ cm}^2 \text{ s}^{-1}$, compared to $L \sim 10^{31}$ of the ISR; scaled up to ISR energy and volume, L would become $\sim 10^{40} \text{ cm}^2 \text{ s}^{-1}$.

To compare the magma parameters with those of plasma devices, one can use the triple product of the ion kinetic energy T_i , central density n_c , and confinement time τ , which was observed to be $T n_c \tau \approx 4 \times 10^{14} \text{ keV cm}^{-3} \text{ s}$; this value is comparable to those achieved in the most advanced plasma fusion machines (fig. 2): JET (Joint European Tokamak) reached $T = 8 \text{ keV}$, $n = 4-5 \times 10^{13} \text{ cm}^{-3}$, and $\tau \sim 1 \text{ s}$ in 1987 or $T n \tau = 3-4 \times 10^{14}$; Alcator C, in 1986, attained $T = 1.6 \text{ keV}$ and $n \tau = 8 \times 10^{13}$ or $T n \tau = 1.3 \times 10^{14}$; and TFTR, in 1987, achieved $T = 1.3 \text{ keV}$ and $n \tau = 10^{14}$ or $T n \tau = 1.8 \times 10^{14}$.

1.1. Plasma parameters of neutralized magma

In contrast to thermal plasmas in a mirror, magma is characterized by (1) highly nonadiabatic large Larmor radius orbits, $a_L \sim \frac{1}{2}R$, where R = plasma radius; (2) zero canonical angular momentum, $P_\theta \sim 0$, giving a centrally peaked radial density distribution of the form (fig. 3)

$$n(r) = r^{-1} (r^2 - R^2)^{-1/2}; \quad (2)$$

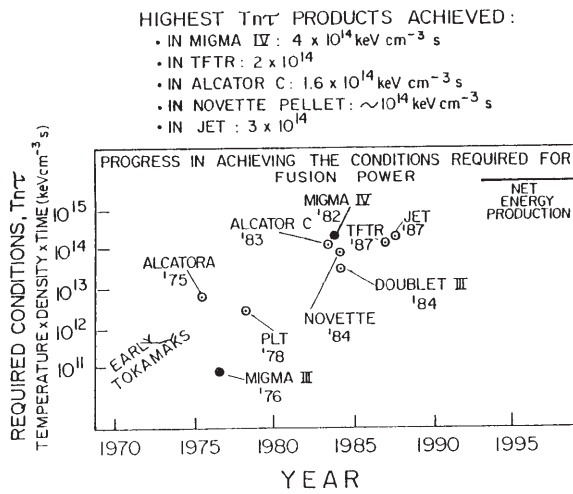


Fig. 2. Progress in achieving the conditions required for fusion power as measured by the triple product temperature \times density \times confinement time.

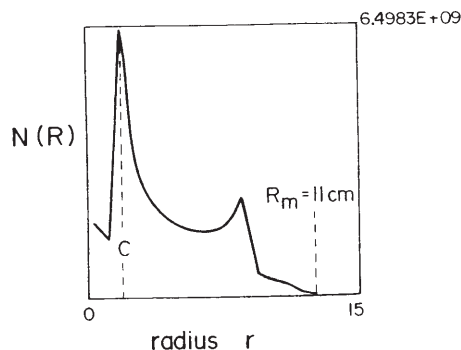


Fig. 3. Migma density profile. The observed number of D^+ ions, N , as a function of the radial distance r from the geometrical center "O". C is the physical center and $R_m = 11$ cm the physical radius. The scale is relative, and the measured peak density = $3.3 \times 10^{10} \text{ cm}^{-3}$.

(3) non-Maxwellian peaked distribution of ion energies, E_i ; and (4) a large ion-to-electron temperature ratio (E_i/T_e), $\sim 10^3$, with $E_i = 650 \pm 100 \text{ keV}$ and electron temperature $T_e = 0.4 \pm 0.3 \text{ keV}$. The magma volume, $V = 135 \text{ cm}^3$, is a disk of $R = 9.3 \pm 0.1 \text{ cm}$ and height $Z_0 = 1 \pm 0.5 \text{ cm}$.

These and other properties of magma are compared with those of plasma in tables 1 and 5. Plasma physics

regimes of the Migma IV experiment in terms of plasma-to-cyclotron frequency ratios were

$$0.2 < \omega_{pi}/\omega_{ci} < 0.5, \quad (3a)$$

$$13 < \omega_{pe}/\omega_{ci} < 27, \quad (3b)$$

for ions and electrons respectively, where an unstable gap against $m = 1$ flute was specifically predicted [5,8].

Migma is formed by collisional dissociation of D_2^+ ions near the center of symmetry of the magnetic field. The vacuum system [9] in Migma IV renders it possible to inject a 0.5-mA dc beam of 1.45-MeV molecular D_2^+ ions, while maintaining $p = 3 \times 10^{-9} \text{ Torr}$ (fig. 4). The trapped d^+ 's travel in precessing, quasicircular orbits of rosette pattern [10,11]. For each orbit, the distance of closest approach to the center of symmetry of the magnetic field, C, is referred to as the impact parameter b (fig. 5); b is defined as positive when the orbit encloses the center. The beam can be cut off in 50 μs to measure the ion confinement time τ . In the typical density growth decay curve (fig. 6), this was done at point B.

1.2. Collisional energy in magma

Although the orbits intersected at all crossing angles, $\theta_{12} = 0^\circ - 180^\circ$, the weighted average crossing angle was

Table 1

Comparison of physical parameters of a mirror containing plasma to those containing self-colliding orbits (magma)

Physical configuration and parameters	Plasma mirror	Self-colliding beam mirror (Migma)
1) Orbit characteristics	adiabatic orbits; gentle variations of B along the particle trajectories	nonadiabatic orbits; large variations of B along the orbits
2) Radial scale length of the magnetic field $R_M = \left \frac{dr}{dB} B \right $	$R_{Li} \ll R_M$	R_M comparable to R_{Li}
3) Ion Larmor radius, R_{Li} compared to plasma radius, R_p	small, $R_{Li} \ll R_p$	large, $R_{Li} \sim \frac{1}{2}R_p$
4) Canonical angular momentum $p_\theta = m_i r (v_\theta + \frac{eA_\theta}{m_i c})$	large; broad distribution	≈ 0 (orbits through or near the axis of symmetry)
5) Radial scale length of density, $a = \left \frac{dr}{dn} n \right $	$a \gg R_{Li}$	$a < R_{Li}$
6) Axial extent	long, many-fold R_{Li}	short, comparable to R_{Li}
7) Radial density distribution	nearly uniform	nonuniform (peaked at center of symmetry)
8) Axial density distribution	nearly uniform	nonuniform (peaked at center of symmetry)
9) Distribution of motions	random (quasi-Maxwellian, of loss-cone type)	quasi-ordered, with large dispersion due to precession, z -oscillations and multiple scattering

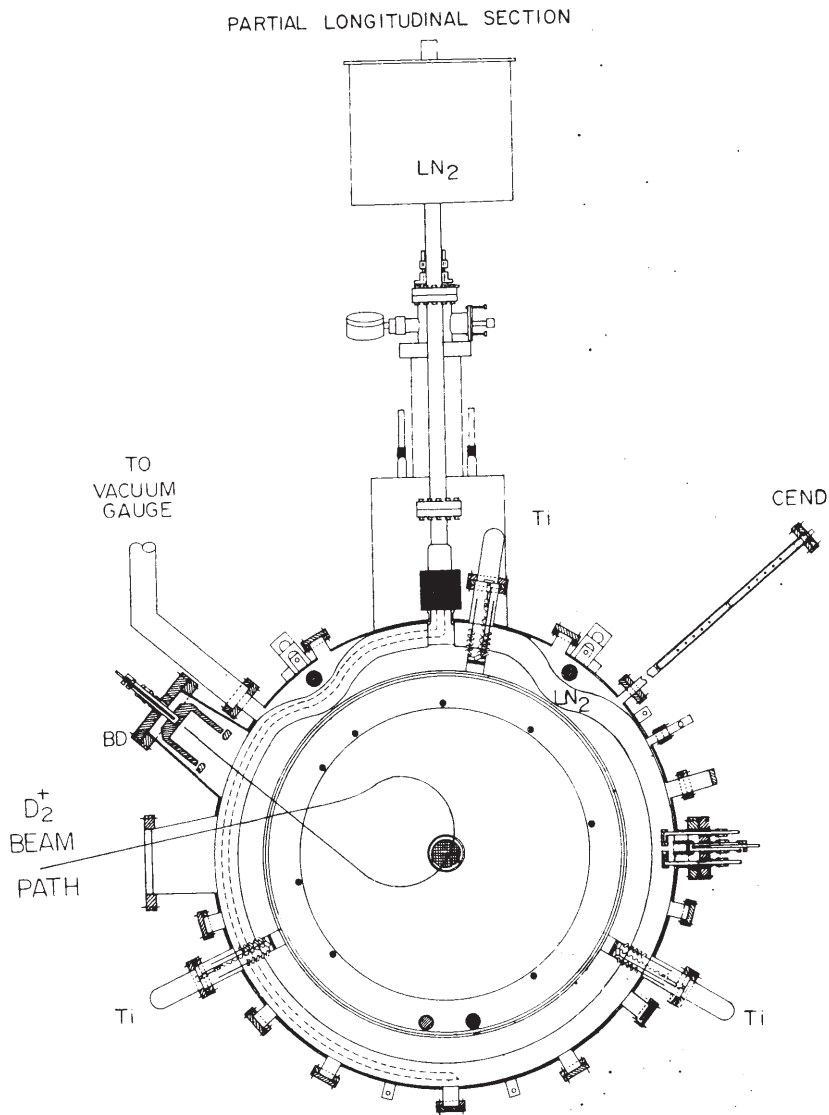


Fig. 4. Cross-sectional drawing through $z = 0$ plane of the chamber. CEND, charge-exchange neutral detector; Ti, titanium sublimation pumps; LN₂, liquid N₂; D⁺, orbits of trapped D⁺ ions; C, center of symmetry $x = y = z = 0$; BD, beam dump.

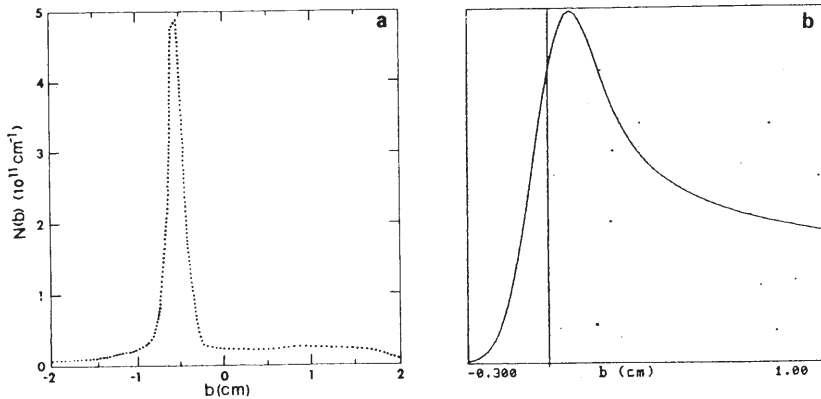


Fig. 5. Number of D⁺ ions vs impact parameter b (distance of closest approach of the magma orbit to the center of symmetry of the magnetic field). (a) Observed distribution. (b) Predicted distribution based on the uniform dissociation of D₂⁺ on the residual gas.

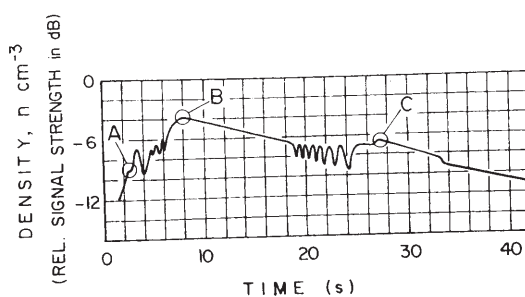


Fig. 6. Migma ion density versus time. Composite tracing of multiple-exposure ion buildup and decay curves, measured by the rf pickup, showing onset of instability at -10 dB during filling (point A is the space charge limit); stable confinement above -6 dB; (point B) stable, nearly exponential decay to -6.5 dB; and unstable decay to -9 dB (point C) followed by stable decay. $U = -225$ V was applied to allow passage through the unstable zone. Signal strength after 24 s was affected by contributions from electrons (observed up to 3 dB with trapping bias applied); all reported N and n results with $U \neq 0$ have been reduced by a factor of 2 to allow for this effect. The space charge limit is at point A (from ref. [1]). The abscissa directly measures the total number of stored D^+ 's in magma, N ; the density is derived on the assumption that the magma volume is constant.

still $\langle \theta_{12} \rangle = 160^\circ$. This is because (i) the flux term β_{12} , eq. (1), favors large θ_{12} , and (ii) the cross section for the reactions considered here increases with β_{12} . That is, effects (i) and (ii) "pick up" mostly collisions with $\theta_{12} = \text{large}$. This is demonstrated in fig. 7.

2. Focusing of magma orbits

2.1. Effective potential surfaces versus mirror ratio

The magma of 0.725 MeV deuterons is formed in the axisymmetric magnetic field of the shape known as the "simple mirror". Its field strength at the center of symmetry, $r = z = 0$, is $B_0 = 3.17$ T; it quadratically decreases with r and increases with z . The field components are given [10] by:

$$B_z(r, z) = B_0(1 - \alpha r^2 + 2\alpha z^2), \quad (4a)$$

$$B_\theta = 0, \quad (4b)$$

and

$$B_r = -2B_0\alpha rz, \quad (4c)$$

with $B_0 = 3.17$ T and the magnetic field index

$$\alpha = k/R^2 = 8 \times 10^{-4} \text{ cm}^{-2}. \quad (5)$$

$k < 1$, which implies "weak focusing" forces. These are provided by the radial component of the field, eq. (4a), which exerts axial focusing force on the large radius

magma orbits away from the midplane, $e\mathbf{v}_z \times \mathbf{B}_r$. This very same mirror field shape provides a stronger confinement (a less open mirror) when the orbits are large than that given by the mirror ratio effect on the adiabatic plasma orbits (fig. 8). The large orbits are not confined by the flux lines but by the effective potential surfaces U_{eff} , given by

$$U_{\text{eff}} = 1/2m(eA/c)^2, \quad (6)$$

where the vector potential is given by

$$A = B_0(r/2 - kr^3/4R^2 + krz^3/R^2). \quad (7)$$

The loss cone is decreased twice as much by the mirror effect in the case of magma's nonadiabatic orbits as it is in the case of adiabatic orbits.

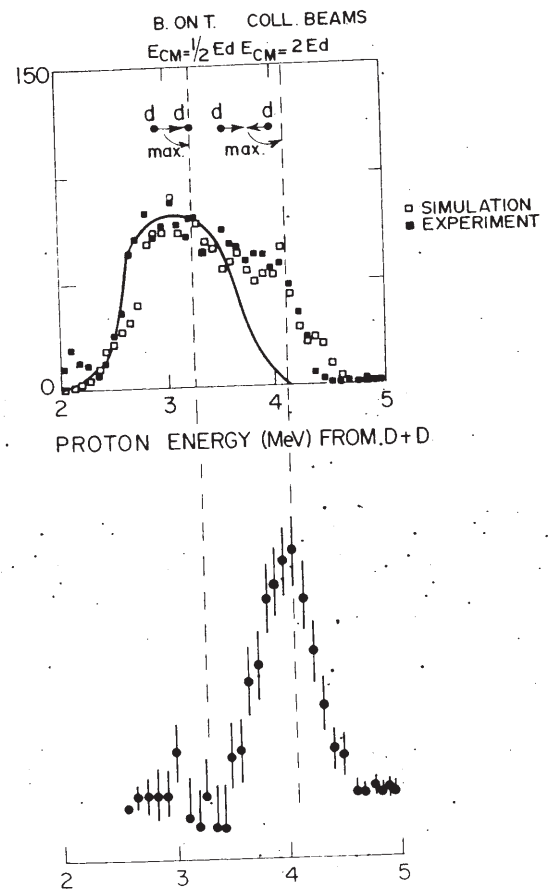


Fig. 7. Top: observed proton energy distribution from $d + d \rightarrow T + p + 4$ MeV is a superposition of beam-on-gas (curve) and beam-on-beam (solid and hollow squares). Bottom: the difference Δ between experimental points (solid squares) and the curve as a function of the colliding beam factor f , which ranges from 1 (target at rest) at the beam-on-gas maximum to 4 (crossing angle 180°) at the beam-on-beam maximum.

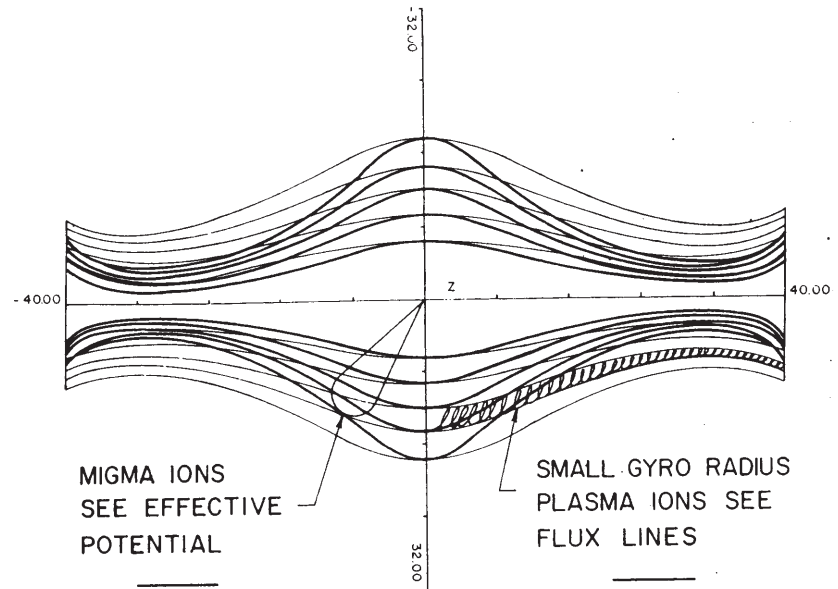


Fig. 8. Difference between a simple mirror and a focusing mirror. The field shape is given by eq. (4). The two sets of lines plotted are the flux lines and the magma energy envelopes obtained from the requirement of conservation of canonical angular momentum, eq. (6), and are the boundaries of magma ions of a given energy. Plasma orbits, on the other hand, will be bound to the flux lines. Magma does not obey the same Alfvén mirror relation that a plasma does.

2.2. Suppression of multiple scattering spread by focusing action in a magma

In addition to the factor of two decrease in multiple Coulomb scattering (MCS) effects in magma due to the mirror effect, there is an additional factor of two suppression from the projection in phase space of the scattering angle. This effect does not exist in adiabatic systems, only in thin beams in cyclic accelerators that undergo axial betatron oscillations. R.A. Miller [12] applied phase space projection to magma. The magma ions also oscillate up and down along the z axis (see characteristic orbit frequencies below), but in a more complicated manner.

In a plot (not shown here) of v_z versus z , where v_z and z are the velocity and distance along the axis, a particle's position and velocity at any given time will be a point on the plane. A harmonic oscillation will traverse a closed curve on the plane that can be made into a circle by the appropriate choice of scales. A Coulomb scattering event will change v_z instantaneously, but not z . At $z = 0$, $|v_z| = \text{max}$, the effect of a small scattering event is entirely in the direction of changing the radius of the circle, which directly affects the maximum z excursions. At $|v_z| = 0$, $|z| = \text{max}$; however, the effect of a small scattering is only a *change in phase* of the orbit. (This can seem counterintuitive unless it is realized that this is for a very small scattering.) Thus, for a harmonically oscillating particle, the scattering in the z

direction averages only half the amount [in $(\Delta v_z)^2$] it would have if unbound.

2.3. Characteristic orbit frequencies

There are four characteristic ion frequencies of magma orbits (three of which are independent): radial, precessional, axial, and cyclotron frequency – ω_r , ω_p , ω_z , and ω_c , respectively, where $\omega_c = \omega_r + \omega_p$. In contrast, thermal plasmas are characterized by only one frequency, $\omega_c \neq 0$. The amplitude of axial oscillations was typically $Z_0 = 0.5$ cm.

The four frequencies are a function not only of the particle energy and B , but also of the impact parameter

Table 2
Magma orbit radial, precessional, and axial frequencies ω_r , ω_p , and ω_z as functions of deuteron energy and impact parameter in magma with $B_v = 3.324$ T

Deuteron energy (MeV)	Impact parameter (cm)	ω_r (MHz)	ω_p (MHz)	ω_z (MHz)	ω_z/ω_r
0.60	0.00	24.43	-0.302	4.03	0.165
0.80	0.00	24.06	-0.430	4.86	0.202
0.60	-2.00	24.73	-0.275	3.74	0.151
0.80	-2.00	24.46	-0.837	4.45	0.182
0.60	2.00	23.83	-0.351	4.54	0.190
0.80	2.00	23.30	-0.506	5.56	0.239

b. For $b = 0$, the calibrated frequency values for a field of $B_0 = 2.883 \pm 0.01$ T are $\omega_c = 21.388$ MHz, $\omega_p = 0.685$, and $\omega_r = 20.70$ MHz. For $B_0 = 3.324$ T, examples of the radial, precessional, and axial frequencies are given in table 2 for two deuteron energies (0.6 and 0.7 MeV) and three values of b (-2, 0, and +2 cm). We note that the well-known single particle resonance in cyclic accelerators is expected for $\omega_z/\omega_r = 0.5$. We also note that while in the accelerator case ω_i is the radial betatron frequency about the equilibrium orbit, in the case of magma it is the gyrofrequency of all motions between C and R_{\max} .

3. The apparatus

The Migma IV experimental apparatus [13] consisted of (a) an injector, which is comprised of an ion source, accelerator, and beam transport system; (b) a vacuum system; (c) a reaction chamber; and (d) a superconducting magnet.

(a) The *injector* delivers 0.5 mA dc of D_2^+ at energies up to 2 MeV to a 0.8-cm spot in the center of the chamber. Other beams are also possible, such as D_3^+ , which, in fact, was used in some of these experiments. (The injector formerly had a pulsing device incorporated into the ion source but this has been temporarily removed.) The ion source is a duoplasmatron type with terminal analysis by means of a permanent magnet type magnetic analyzer after beam extraction. The ion source region is independently pumped by a Ti-Ball sublimation pump to improve beam quality and accelerating tube performance. It also incorporates two Einzel type lenses, one of which serves to match the source optics to the accelerator tube optics. The ion source is cooled by an external freon cooling system and all internal controls are by standard Sel-Syn's.

The *accelerator* is a standard High Voltage Engineering Corp. Model KN-3000, modified to accept this new ion source and the increased terminal weight. Down charge was added to increase the current capacity, as was a sulfur hexafluoride gas handling system. Column current was increased to "stiffen" the beam. Stability is maintained by a generating voltmeter feedback loop to the corona points. Typical beam energy and current during the Migma IV experimental runs were 1.4 MeV and 0.3 mA D_2^+ respectively, with a maximum beam in the reaction chamber of 0.5 mA at 1.4 MeV; D_3^+ at 1.2 MeV and 0.08 mA was also injected.

The *beam transport* to the reaction chamber is made by way of an electrostatic and magnetic optical system. This includes initially an electrostatic x-y steerer at the base of the accelerator, followed by an electrostatic quadrupole triplet. The beam next passes through an analyzing magnet and is deflected 25°, then through another electrostatic quadrupole triplet and through a final steerer before entering the reaction chamber. Due

to the power in the beam and small spot size, all the optical elements are protected by liquid-cooled apertures, and several critical areas on the reaction chamber are monitored by heat sensors to protect against accidental burnthrough.

At various locations along the beam path, Faraday cups with a 1:1.5 aspect ratio and apertures were installed to monitor beam current and to gain some beam profile information. A ceramic break for electrical (mainly noise) isolation was installed between the second quadrupole and the analyzing magnet. All Faraday cups and apertures were biased at +100 V to suppress e^- emission.

A beam switcher or deflector (D_1) is located just after the analyzing magnet. This deflects the beam off the hole through aperture A_1 from full beam to essentially zero current in 30 μ s. Due to the local heating caused by the small beam spot size (less than 2 mm FWHM) and beam power (750 W), as soon as this deflection is completed, Faraday cup F_0 is inserted to intercept the full beam before the analyzing magnet and thereby take the thermal load off A_1 and decrease the gas load to this region of the system, while maintaining switching speed. To reinject the beam, the Faraday cup is withdrawn and the deflector then allows the beam to pass through A_1 after a 500 ms delay, with a beam "turn-on" time (FWHM) of 50 μ s.

(b) *Vacuum* is maintained by a multistaged pumping system [9] consisting of oil diffusion pumps and titanium sublimation. The first stage is the standard accelerator vacuum system, which is non-bakeable and O-ring sealed. This is pumped by a liquid nitrogen trapped oil diffusion pump. The second stage begins at the analyzing magnet, and, from this point on, the beamline is copper gasket sealed and bakeable to 400 °C. An isolating orifice after the analyzing magnet limits gas flow from the first stage to the second. The second stage was pumped by two liquid nitrogen trapped oil diffusion pumps, but will be converted to cryopumps. The vacuum in the first stage was typically a few $\times 10^{-7}$ Torr and in the second stage is a few $\times 10^{-9}$ Torr. The third stage consists primarily of the reaction chamber. It is pumped by means of titanium sublimation. The periphery of the chamber consists of a liquid nitrogen cooled baffle onto which titanium is evaporated. The calculated pumping speed along the periphery is approximately 100 000 liters/s. The chamber is conductance-isolated from the beamline by the beamline itself, and the normal dynamic vacuum of the chamber was a few $\times 10^{-9}$ Torr (principally D_2); in some runs, it was $\sim 10^{-8}$ Torr.

There is a significant gas load presented by the beam in the chamber itself. The best static vacuum obtained in the chamber was 5×10^{-12} Torr after baking at 450 °C for 24 h with no injected beam. All vacuum measurements are made with trigger discharge gauges and with an accuracy of about $\pm 50\%$. Background gas

slotted are
entum, eq.
es. Migma

$(\Delta v_z)^2$ it

encies of
t): radial,
 ω_r , ω_p ,
In con-
only one
scillations

nly of the
parameter

ries ω_r , ω_p ,
t parameter

ω_z/ω_r

0.165
0.202
0.151
0.182
0.190
0.239

analysis is monitored (although not optimally) by a magnetic sector residual gas analyzer located at the end of a long pipe connected to the chamber (kept so far away due to the large magnetic fields generated by the magnet affecting the analyzer).

(c) The *reaction chamber* (fig. 4) is a stainless steel vacuum vessel sandwiched between two superconductive magnets with various ports and feedthroughs for instrumentation. Two high-powered liquid-cooled Faraday cups are used as beam dumps (one at 0° or field off position and one at 205° or field on position). These contain either apertures at 0° or slits at 205° , which give beam profile and position data. Along the z magnetic axis, which is horizontal, are two instrumentation ports. These contain three surface barrier detectors for nuclear reaction products and rf pickup plates. There are also three baffled titanium filament sublimation assemblies mounted along radial ports that are periodically fired as needed to maintain the desired vacuum. The chamber and beamline from the analyzing magnet to the chamber can be fitted with baking mantels. During the baking process the magnet must be separated and the chamber externally supported (fig. 9).

(d) *Superconducting magnet.* The field in eqs. (4) was produced by two pairs of superconducting solenoid-type coils mounted in separate dewars [14]. The coils are

constructed of approximately 8000 turns of niobium titanium multifilament wire in a copper matrix. This configuration produces a peak field on the conductor of 6 T, a peak field along the z (coil) axis of 3.85 T, and a central field of 3.5 T; the mirror ratio is approximately 1.024:1 over the confinement volume. The magnetic field is designed to allow the chamber to have an inside z dimension of 7.5 cm. Each coil has a center tap that allows shaping (making the field more uniform by reducing the central value) of the field to study and optimize ion orbit behavior.

Let I_M be the magnet current (in A) in the outer coil set, $I_M - I_T$ the current in the inner (I_T is the "trim" current). We concentrate on small r and z where, for constants B_0 and α , eq. (1) is valid.

Combining numerical integrations, we found

$$B_0 = (2.889 I_M - 1.961 I_T) \times 10^{-2} \text{ T/A}, \quad (8)$$

$$\alpha \approx 8.44 \times 10^{-4} \frac{I_M - I_T}{I_M - 0.68 I_T} \text{ cm}^{-2}. \quad (9)$$

Example: $I_M = 122$ A, without trim, would give a central field of 3.52 T and $\alpha = 8.4 \times 10^{-4}$ (for any I_M). Adding 22 A of trim reduces the central α field by 12% to 3.09 T and reduces α by 7% to $7.88 \times 10^{-4} \text{ cm}^{-2}$.

The coils operate at 4.2 K in a boiling liquid helium bath powered externally through counterflow cooled

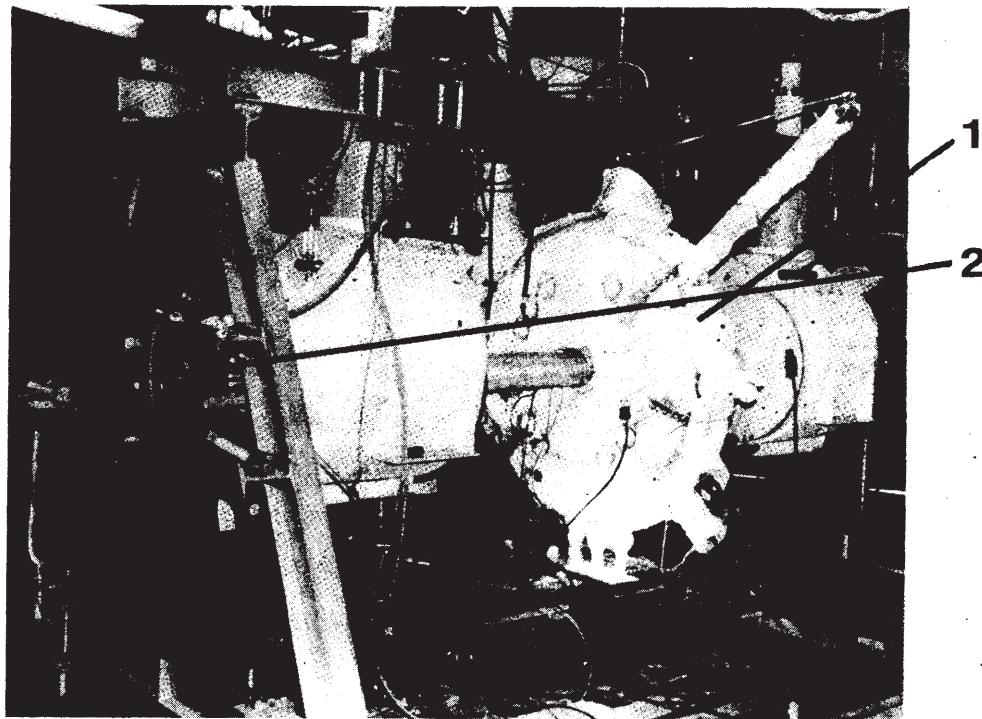


Fig. 9. Baking of the magma vacuum chamber (1) at 450°C . The 25 cm diameter axial tube is welded to the chamber and the two superconducting coil pairs slide away from it, supported by braced holders (2) on each side.

lead
115
arab
bers
ture
has
these
mag
liqui
level
field
“gin
be e.

Fig.
the k
whic
abou
one
thus
this j

niobium trix. This inductor of 5 T, and a approximately magnetic an inside r tap that rm by re-study and outer coil he "trim" where, for nd
(8)
(9)

ld give a r any I_M .
ld by 12%
 $^4 \text{ cm}^{-2}$.
id helium
ow cooled

leads. Typical operating currents were approximately 115 A. Because of the independent cryostats and separability of the magnets, significant supporting members must be transferred from liquid helium temperature to room temperature. The heat load caused by this has been managed by a counterflow tracer tube along these members. The nominal helium consumption of the magnets is 5 liters/h at field. A permanent low loss liquid helium transfer system is used to maintain liquid levels during operation by remote periodic filling at field. The magnet and chamber are both mounted on a "gimballed" structure that allows spatial orientation to be easily changed and optimized.

A photograph of the magnet-chamber assembly is shown in fig. 10.

4. Diagnostics

Three nondestructive diagnostics were used:

(1) An rf pickup system [15,16] measures the number of trapped ions N at any time, and, consequently, τ . Schottky noise produced at frequency ω is picked up on a pair of plates of radius $\frac{1}{3}R$ placed at $z = +3.75$ and -3.75 cm. The observables are frequency-power spectra $P_r(\omega)$ and $P_z(\omega)$, where r and z refer to radial (com-

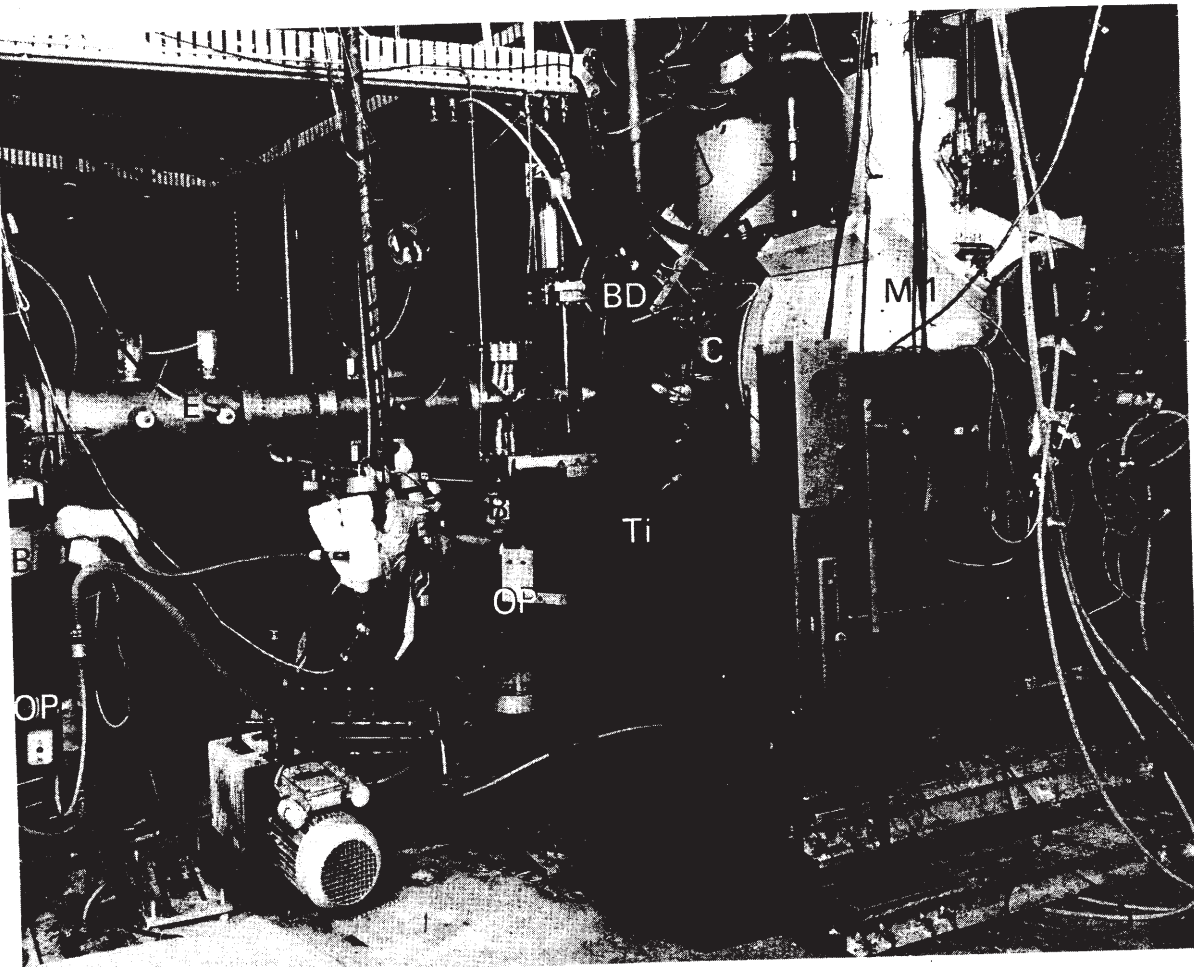


Fig. 10. Migma IV apparatus. The D_3^+ beam enters the experimental area from the left (arrow). With the magnetic field turned off, the beam would pass straight through the chamber C. When the superconducting magnetic coils M1 and M2 (not seen) between which the chamber is sandwiched are fully powered, the field on the conductor is about 6 T, and in the midplane between the coils, about 3.3 T. A water-cooled beam dump (BD) is placed to absorb the undissociated part (99.9%) of the beam. Three titanium pumps, one of which is seen marked Ti, coupled with the diffusion vacuum pump, provide a pumping speed of 10^5 liters/s in chamber C, thus maintaining a pressure of 10^{-9} Torr, with the beam hitting BD. Cables from the inside detectors, both rf and nuclear, exit from this part and a similar one at the other side. CEND is the neutral particle detector. Two oil diffusion pumps (OP) with baffles (B) are seen. ES is the electrostatic quadrupole triplet.

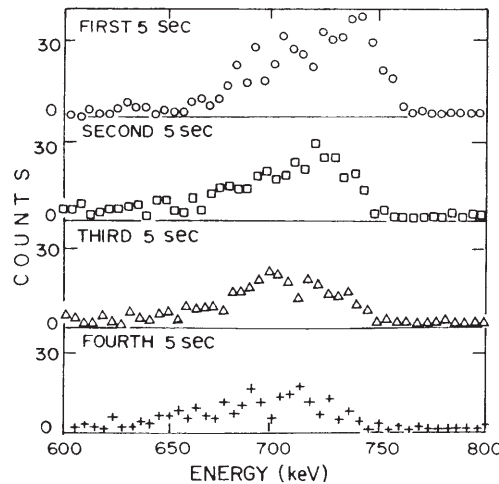


Fig. 11. Energy confinement time. Charge-exchange spectrum sequence versus time: four spectra acquired in four time intervals of 5 s each during ion-number decay with $U = -220$ V, showing $dE_i/dt = -2$ keV/s.

mon mode) and axial (differential). The distribution in b (fig. 5a) is calculated from P_r . $\langle Z_0^2 \rangle$ is inferred from P_z . A variable dc bias U up to ± 1.0 kV is applied on

each of the pickup plates. As it turned out, U was crucial in forcing the electron oscillations out of resonance with the ion cyclotron frequency, which provided the stable neutralized system.

(2) A CEND [16,17] measures the number and energy of neutralized deuterium atoms to obtain N , E_i , and the ion energy-loss rate dE_i/dT (fig. 11).

(3) A nuclear particle detector system [16,17] measures the proton and triton rate and energy from the $D(d, p)T$ reaction and distinguishes p 's produced in fast + fast ($d^+ + d^+$) reactions from those in fast + slow ($d^+ + D^0$) gas reactions (fig. 12).

No T_e diagnostic was installed; the range of T_e was inferred from the rf system's response to change of U (sec. 13).

Details of the diagnostic systems, condensed from ref. [13], are given in sections 5–7 below.

5. RF spectra

The rf apparatus used [16] in Migma III was modified to allow separate observation of radial and axial ion motions. The bandwidth was increased so that the first three harmonics of radial motion frequency, along with any associated sidebands, could be observed. Observed rf signals were strong enough to allow us to dispense with the resonant lines used in earlier experiments to maximize signal to noise ratio. The amplification of the system was constant within ± 1.0 dB over a 60 MHz bandwidth, which greatly simplified interpretation of the data. In addition, it allowed observation of details in the spectrum that could not be easily observed previously.

By adding the signals from two plates, an improvement of 3 dB in signal to noise ratio was obtained for the radial signal, from which the impact parameter distribution is calculated. At the same time, any misleading signals present due to axial motion were rejected by 20–30 dB. The signals from the two plates were separately subtracted, giving a spectrum from which the axial spreading of the magma distribution could be derived. The measured sensitivity of this technique corresponds to an amplitude of 0.5 cm p-p (peak-to-peak) for 5×10^9 ions. If 5×10^{11} ions had an average amplitude of 0.05 cm p-p, they would produce an observable signal. This was calibrated by injecting the beam with a controlled amount of axial misalignment and measuring the resulting signals. The axial amplitude was independently calibrated.

This high sensitivity is due in part to a relationship between the axial (ω_z) and radial (ω_r) frequencies of ion motion. As a function of impact parameter, ω_r increases while ω_z decreases. Consequently, the sum frequency (the upper axial sideband of the fundamental radial frequency) is nearly independent of impact

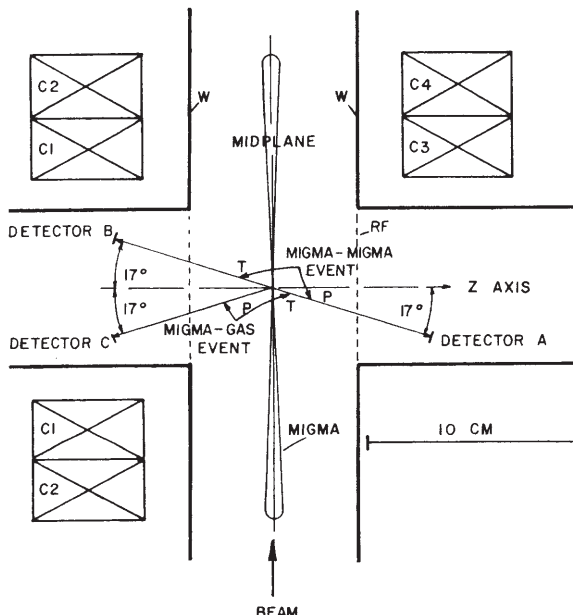


Fig. 12. Nuclear particle detector geometry. The magnetic field is horizontal. Detectors A and B measure protons and tritons emitted back-to-back from $D + D \rightarrow T + P + 4$ MeV from $D(\text{migma}) + D(\text{migma})$ event. Detectors A and C detect protons and triton from $D(\text{Migma}) + D_2(\text{gas})$ events. W = wall of the chamber. RF = metallic mesh for rf signal pickup; C1 and C2 = NiTi coils from left side magnet; C4 and C5 = same from right side (lower section not shown).

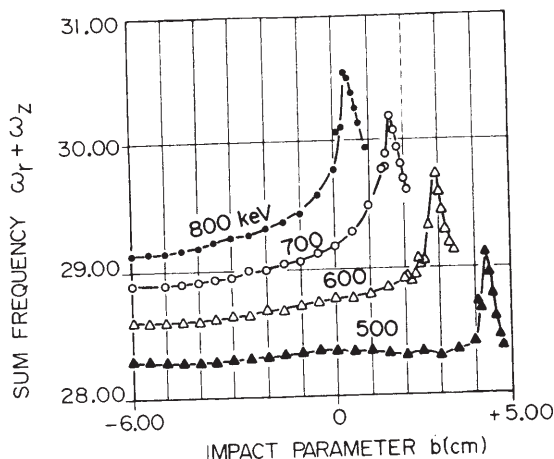


Fig. 13. The sum frequency $\omega_r + \omega_z$ (upper axial sideband of the fundamental radial frequency) vs impact parameter b , for several Migma D^+ energies. As a function of b , ω_r increases while ω_z decreases. Consequently, the sum frequency is nearly independent of impact parameter. In some cases the cancellation is over 90% complete; thus, the rf power due to all ions is confined to a small bandwidth yielding a considerable enhancement of the available signal-to-noise ratio.

parameter (fig. 13). In some cases the cancellation was over 90% complete; thus, the rf power due to all the ions was confined to a small bandwidth yielding a considerable enhancement of the available signal to noise ratio. In order to determine axial amplitude as a function of impact parameter, one must measure the spectrum of the upper axial sideband of the second radial harmonic and compare it with the spectrum of the radial fundamental. Although the cancellation of axial and radial frequency dependence upon impact parameter is observed both experimentally and numerically, there is no explanation of why it occurs and no model saying it must occur. It remains to be determined if this effect is merely an accident of injection geometry and field shape or a characteristic of all Migma systems. Experimentally, field shape and injection geometry were varied over the entire range available, with little effect.

The radial rf signal has a peak associated with the impact parameter of the injected beam. At larger impact parameters, the signal strength falls off until a shoulder is reached beyond which no trapped ions are observed. Calculations and experimental observations confirm that this shoulder corresponds to the limit of confinement due to the 2:1 resonance zone. The observed axial signal has a peak that is always present, even with the best midplane injection. This peak is identified with ions being continually injected near this resonance and lost out the loss cone. They always reach a large axial amplitude and, therefore, produce a strong signal. The actual number of ions involved, however, is quite small (of the order of 1%).

The radial signals, under certain circumstances, showed extra structure consisting of a number of wiggles with a spacing of 100–200 kHz. This structure is more evident when a large number of ions is confined. For any given set of injection conditions, the wiggle spacing is independent of all other parameters. Their amplitudes were dependent on the trapping bias U , adjustable from 0 to -1000 V applied to the rf pickup plates, and the amplitude of induced axial oscillations. They have been observed [16] with Migma III; however, with lower beam power, it was possible to alter injection conditions so that they were not present. The wiggles may be symptomatic of enhanced losses.

6. RF lifetime

In most cases, it was possible to obtain meaningful lifetime results from the radial rf signals (fig. 6). Measurements were made on both the decaying rf spectra and on a broadband signal that included, simultaneously, contributions from all trapped ions. The longest lifetime observed was 45 s. The decay was purely exponential if the electrons were trapped by a high trapping bias, $U \leq -300$ V. Without the bias the decay started slowly and later sped up, perhaps due to ion energy loss to electrons. Buildup studies were less conclusive. Excess noise due to the beam made it difficult to observe a clear exponential region of buildup before saturation.

While the radial signal decayed in a normal manner, the axial signal was unusual in its decay characteristics. In one case, with only a small number of trapped ions, the axial signal corresponding to ions away from the 2:1 single particle orbit resonance was observed to grow while the number of trapped ions decayed by an order of magnitude. It seemed that the process of injection maintained a thin distribution that started to spread after the injection stopped. In another case, with almost two orders of magnitude more trapped ions, the axial signal did not decay at all until near the end of the radial decay. The ion number (ion density), deduced from the observed proton counting rate and the D_2 background density (derived from the ion lifetime, assuming the only background gas is deuterium), is consistent with the number obtained from the rf measurements.

7. CEND

A charge exchange neutrals detector (CEND), which consists of a silicon surface barrier detector, is mounted at the end of a collimating tube connected to one of the radial ports looking at the center of the chamber (fig. 4). The distance between the detector and the center of the

chamber is about 141.5 cm. The location of the CEND is such that the neutrals (D^0) produced by the dissociation of the injected D_2^+ beam will not be detected. The CEND will see a fraction of the confined atomic ions D^+ ion the central region of the chamber that are converted to neutrals (D^0) due to the charge transfer process with the background gas or by electron capture.

8. Nuclear diagnostic

The nuclear diagnostic system consists of silicon surface barrier detectors, positioned to detect charged fusion products in coincidence, and associated electronics. A schematic drawing of detector A, B, and Z positions in the Migma IV chamber is shown in fig. 12. The nuclear detection system differs from the Migma III system [16] in that the A detector has been collimated so that it views only particles originating in the central region of the chamber, ~1 cm diameter at the midplane. In addition, constant fraction discrimination was incorporated into the timing system, reducing walk and jitter to 200 ps from the 5 ns observed with the Migma III system.

Three silicon surface barrier detectors with an effective surface area of 25 mm² and depletion depth of around 300 μm were used.

Individual spectra of detectors A, B, and Z observed during several runs are added together. The spectra for an injected D_2^+ energy of 1.445 MeV and a total counting time of 5000 s are shown in fig. 7.

9. Formation of magma and the measured densities

The observed distribution of loci of the D_2^+ dissociation was sharply peaked for orbits passing within $b = 0.2$ cm of the center of a migmacell (fig. 5a). A two-step dissociation mechanism is postulated to explain the observed distribution: first, a "seed" magma of D^+ ions is formed by the combined effect of D_2^+ collisions on background gas, D_2^0 , and, perhaps, Lorenz dissociation; then, the seed magma acts as a target for the D_2^+ beam; this, in turn, results in an exponential magma density growth and thus gives rise to the sharp distribution in b . Without this mechanism, the distribution would be much broader, incompatible with our observation in fig. 5b. At the average volume density of 3×10^9 cm⁻³, only 10^{-5} of the D_2^+ beam gets dissociated; the undissociated D_2^+ beam hits the beam dump (BD in fig. 4).

In one test, D_3^+ ions were injected in an attempt to alter orbit parameters to eliminate the "wiggles" in the rf spectrum (sect. 5). Trapping of deuterons was extremely successful, but the beam energy had to be made too low for a reasonable lifetime (which is proportional to $T^{3/2}$). D_3^+ injection may be preferred.

Ion orbit distributions are inferred from frequency spectra of the ion Schottky noise obtained with the rf pickup system. With 0.36 mA injected 1.45 MeV D_2^+ current and background pressures $< 5 \times 10^{-8}$ Torr, a sharply peaked rf spectrum distribution was obtained. $N = 7 \times 10^{11}$ ions were trapped; 4.4×10^{11} of them had orbits with impact parameters b (distance of closest approach to the axis) within $b_{\text{peak}} \pm 2$ mm. The number of ions per unit impact parameter changes by a factor of 50 as b changes from b_{peak} to $(b_{\text{peak}} + 3.5)$ mm. b_{peak} is controlled by steering the D_2^+ beam. Ion numbers determined from the rf diagnostic giving $n_v \approx 3.2 \times 10^9$ cm⁻³ (plasma volume average) are consistent with those obtained from the observed magma-magma and magma-gas fusion rates. The estimated "midplane" or "central fast ion" density is $n_c \approx 10^{10}$ cm⁻³ (3 × volume average). The central peak density is of the order of $10 n_v$; $n_c \approx 3 \times 10^{10}$.

10. How the space charge limit was exceeded

The space charge limit for nonrelativistic magma is [11]

$$N_{sc} = \frac{5.17 \times 10^8 k T^{3/2} m^{1/2}}{B_0}, \quad (10)$$

where $k = \alpha R^2$, B_0 is in tesla, T is in keV, and m is in amu. At $R = \frac{1}{2}R_m$, $k = 8 \times 10^{-4} (9.3/2)^2 = 0.0173$. For $B_0 = 3.3$ tesla, $T = (1.45/2)$ MeV = 0.725 MeV, $m = 2$,

$$N_{sc} = 6 \times 10^{10}, \quad (10a)$$

or with $V = 136$ cm³, the space charge limit to the density is

$$n_{sc} = N_{sc}/V = 4.4 \times 10^8 \text{ cm}^{-3}. \quad (10b)$$

10.1. Experimental facts

Every time the D^+ density reached $n = 3 \times 10^8$ cm⁻³, which was about 70% of the space charge limit, attempts to further increase n by the continuous injection of D^+ 's resulted in intense bursts in the rf spectrum. The magma orbit pattern (rosette in fig. 1b) and the dissociation peak (fig. 5a) would be destroyed (point A in fig. 6). A negative potential was then applied to two plates of radius $\frac{1}{3}R$, placed 3.75 cm above and below the magma plane and parallel to it. By trial and error a voltage, $U = -300$ V, was found at which the bursting ceased. With this voltage, a nine times higher volume average density than the space charge limit, eq. (10b), was reached without instabilities,

$$n_v = (2.3 \pm 0.21) \times 10^9 \text{ cm}^{-3}, \quad (11)$$

which corresponds to a central density of

$$n_c = 2 \times 10^{10} \text{ cm}^{-3}. \quad (12)$$

What is the physics underlying this observation? Explanations of "bursting" in terms of collective instabilities of the Harris type and other complex effects have been put forth. The bursting could be a simple space charge effect, however. If the magma ion density growth rate \dot{n}_d is greater than the electron density growth rate within the magma volume, \dot{n}_e ,

$$\dot{n}_d - \dot{n}_e > 0, \quad (13)$$

so that every time the excess of ions exceeds the space charge limit

$$n_d - n_e \geq n_{sc}, \quad (14)$$

it would result in electrostatic expulsion of the deuterons from the magma volume. In the rf spectrum it will be observed as "bursting" because the orbits have been destroyed. The fact that the sidebands of the precessional frequency were observed during the bursting (see below) also supports the space charge limit explanation because the rate of mixing is determined by ω_p .

10.2. Ion trapping rate in magma

To compute \dot{n}_d , let I represent injected beam current, \dot{n}_d the number of particles added to the magma per second, σ_D the dissociation cross section for beam on magma, and L the effective beam path length. The number of particles lost per second will be equal to the number added in steady state:

$$\dot{n}_d = N/\tau = I\sigma_D L \lambda n, \quad (15)$$

where λ represents the ratio of beam-average density to n and τ is the time constant for loss, in this case the time constant for scattering out the loss cone.

The beam injected beam current was about 0.5 mA, corresponding to 3×10^{15} particles per second. We estimate [13] that $\sigma_D L \lambda = 6 \times 10^{-15} \text{ cm}^3$, so that at a point in time halfway between A and B (fig. 5) where $n = 10^9 \text{ cm}^{-3}$, eq. (15) gives

$$\dot{n}_d = 1.8 \times 10^{10} \text{ s}^{-1}. \quad (16)$$

10.3. Time average neutralization of magma

Let us calculate the rate of electron production, \dot{n}_e . It is given by

$$\dot{n}_e = n_0 \sigma_i V_d n_d. \quad (17)$$

We assume a vacuum of 10^{-8} Torr, which means that the neutral deuterium gas density $n_0 = 3.5 \times 10^8 \text{ cm}^{-3}$. The ionization cross section is $\sigma_i = 10^{-16} \text{ cm}^2$, and the ion velocity $v_i = 8.2 \times 10^8 \text{ cm/s}$. We find [13] that one magma ion produces 30 electrons per second, or, with $n = 10^9 \text{ cm}^{-3}$,

$$\dot{n}_e \approx 30 n_d \text{ s}^{-1} = 3 \times 10^{10} \text{ s}^{-1}. \quad (18)$$

The comparison of results (16) and (18) suggests at first sight that the electron production rate is comparable to or higher than the magma ion population growth rate, and that the bursting conditions (13)–(14) thus appear not to be satisfied. The comparison is meaningful, however, only if it assumes that all the ions and electrons produced in magma are confined within magma. While this may be true for ions, the classical electron confinement time τ_e is extremely short. For $n_e = 10^9$, $T = 200 \text{ eV}$, and mirror ratio $R = 1.02$, we get

$$\tau_e = 3.44 \times 10^5 T_e^{3/2} \log_{10} R = 10^{-5} \text{ s}. \quad (19)$$

Hence, the electrons will be ejected in the $+z$ and $-z$ directions at a rate comparable to that of \dot{n}_e . Unless the electrons are prevented from exiting axially through the loss cone, the burst condition given by eq. (14) is satisfied.

The negative potential does just that. It bounces the exiting electrons back to the $z = 0$ plane. They begin to oscillate at a natural frequency, which happens to be the ion cyclotron frequency (our observation). Hence, the electrons oscillate through the magma ions as in a Barkhausen's oscillator, a triode, whose grid is positive and whose anode and cathode are at a negative potential. Here, the magma acted as a virtual positive grid. The oscillating frequency is proportional to the cathode-grid voltage, V_{cg} . At low V_{cg} , the electrons pick up the ion gyro frequency, ω_r . This results in the electron-ion resonance which, in turn, ejects the electrons from the magma plane and brings back again the bursting condition eq. (14). By increasing V_{cg} to 300 $V + V_g$, ω_e increases away from ω_r . When the two frequencies are clearly separated, the system becomes decoupled and stable and the peak density is reached (point B in fig. 6).

Such time average neutralization of magma was proposed [18] soon after the first observation of magma. It was argued that each arrival of the electrons at the cathode represents a new initial condition, and a controllable one, too; thus, the two-stream instability will not have time to grow. At that time, a more complex system was believed necessary: a hot cathode and, on the opposite side of magma, the space-charge-limited virtual cathode (fig. 14).

10.4. The rf bursts

After the burst was over, the sharp peak in the magma ion distribution would be greatly attenuated. An examination of the frequency characteristics of the burst indicated that, in the small signal regime, the distribution tended to certain discrete frequencies separated from each other by approximately 0.63 MHz. The lowest of these frequencies was, itself, approximately 0.63 MHz above the frequency corresponding to the ion peak. This is similar to the Harris instability [3], an electrostatic

instability known from other mirror experiments; however, the frequency relationships are different in our case. While one expects [7] the dominant frequency ω_z with sidebands of ω_r , we found sidebands of $(\omega_c + n\omega_p)$. Fig. 15 shows the frequency spectrum of this instability in the small signal regime during ion density buildup and decay. The exact electron bounce frequency is a critical parameter; the application of the correct voltage could tune the electrons out of resonance with the peak of the ion distribution. This is how it was possible to reach stable densities an order of magnitude in excess of the burst threshold.

The peak density is shown by point B in fig. 6. At that point in time, since the continuous injection did not result in further density increase, the beam injection was stopped to measure the migma lifetime. The observed peak density was limited by the injection current deliverable by the accelerator (which could not exceed 0.5 mA), rather than by any instability. The observed decay time ranged from 20 to 45 s, and it can be fully accounted for by the D⁺ charge exchange interaction with the residual gas (sect. 12).

The slow oscillations between points A and B are explained by the neutralization process. The supply rate of electrons through the ionization of the residual gas by the migma ions is a periodic function because the ionization destroys the source of electrons – gas molecules – and it takes seconds for the system to receive new residual gas (from the gas released from the chamber surfaces).

As a result, we would qualitatively expect an exponential growth, modulated by a periodic function whose period corresponds to the residual gas influx time

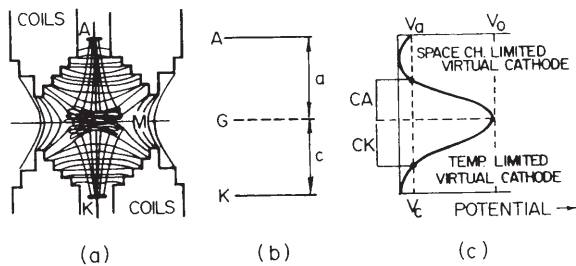


Fig. 14. Early concept of time average neutralization of migma by oscillating electrons. (a) Migma M in midplane between a pair of superconducting coils (COILS) with the equipotential lines of the magnetic field (not the flux lines) drawn; A = anode, K = hot cathode. A is somewhat farther away from the midplane than K to allow for accumulation of the electron space charge and the formulation of a space charge virtual cathode. (b) The equivalent triode with G = grid = migma and $a > c$. (c) Distances vs potential. CA = distance grid-to-virtual-cathode near anode; CK = grid-to-temperature-limited-virtual-cathode near hot cathode. V_a = external anode potential; V_c = external cathode potential. The system oscillates between two cathodes when $CK > CA$ and $V_a > V_c$.

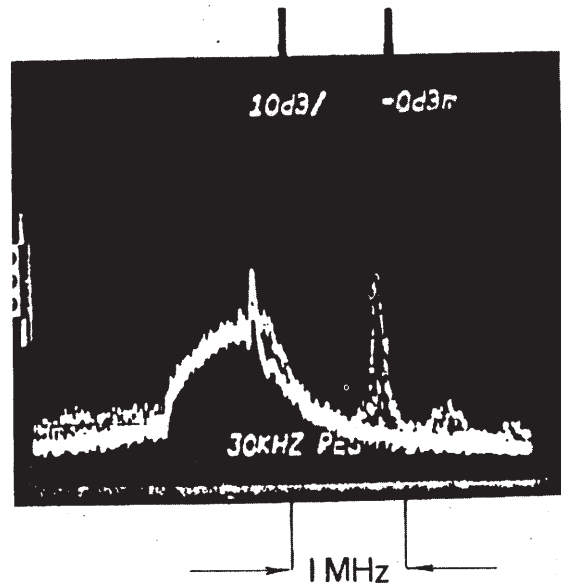


Fig. 15. Multiple exposure showing, on the left, the broad peak of the migma ion rf noise spectrum with the superimposed sharp peak corresponding to injection impact parameter and, on the right, low level (near instability threshold) rf peak attributed to axially oscillating electrons. Electron spectrum has strong components at $\omega_c + \omega_p$, $\omega_c + 2\omega_p$, etc. Note possible rf activity at the right hand side shoulder of the ion spectrum; this would be near $\omega_c - \omega_p$ (ω_r). Lower frequency sidebands of ω_c , if present, would be obscured by the ion spectrum.

constant (1–3 s). This is in good agreement with the shape observed in fig. 6.

Similar oscillations on the decay side can be explained as due to the buildup of excess electron charge as the ion number decreases. The bump at C in fig. 6 was shown to be due to the electron signal when the electron frequency dropped (due to the depletion of the source of the positive potential, i.e., the migma) and came near the ion cyclotron frequency, to which the pickup circuit was tuned.

11. Density buildup and exponentiation process

The ion impact parameter distribution expected from gas dissociation without experimentation is shown in fig. 5a, compared to the actual impact parameter distributions shown in fig. 5b. The extremely sharply peaked impact parameter distributions observed strongly suggest the exponentiation process. Several processes can contribute to trapping of deuterons. Gas dissociation is most important at high pressures. Under good vacuum conditions, other dissociation mechanisms become important. Our observation is compatible with

beam-magma collisional dissociation and beam-electron collisional dissociation being the dominant mechanisms responsible for exponentiation. Lorentz dissociation has not been ruled out as a trapping mechanism, although it is difficult to see how it can lead to the sharply peaked distributions observed.

12. Measurement of the energy confinement time and energy loss rates

Ion storage time and energy loss rates were independently determined from CEND. Observed energy confinement times range from 20 to 45 s.

Energy spectra from the CEND typically have a sharp upper edge and a tail extending to lower energies (fig. 16). The magma ions of 725 keV typically lose 36 keV or 5% during their lifetime of 20 s, or 1.8 keV/s (fig. 11). The lifetime and energy loss are a weak function of the density. The deuteron injection energy corresponds to the peak near the upper edge. By synchronizing the CEND data acquisition with the beam cutoff, it was possible to observe the spectra of ions lost at various times during the particle decay. Typically spectra were taken during four five-second intervals as the ion number decayed. The loss of ion energy was clearly evident. Simultaneously, rf spectra were recorded. The ion lifetime derived from the CEND decay was typically larger by 30% than the corresponding lifetime derived from the rf spectra. This discrepancy may be explained by a misalignment and the anomalous axial spreading of the distribution observed with the rf system.

Analysis of energy loss shows that magma-gas collisions are marginally sufficient to explain all the observed loss. It is quite possible that ion-electron collisions

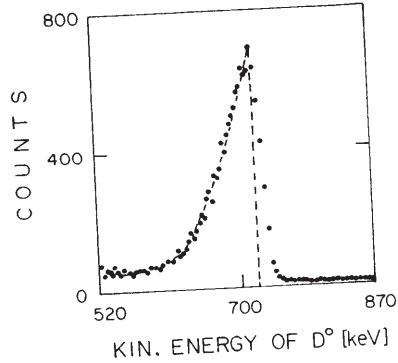


Fig. 16. Energy spectrum of the neutrals from D^+ (fast) + D_2^0 (gas) $\rightarrow D^0$ (fast) + D_2^+ observed in CEND. The dashed line is the computed spectrum assuming 3 keV/s energy loss to electrons in addition to ionization loss to background gas. The slope towards the low energy end fits well with the energy dependence of the charge exchange cross section, eq. (21).

Table 3
Charge transfer cross sections in units of 10^{-19} cm^2 for three values of deuteron kinetic energy

Target	0.6 MeV	0.7 MeV	0.8 MeV
H_2/D_2	2.4	1.1	0.57
He	7.0	3.0	2.0
N_2	30	18	12
O_2	50	22	15
H_2O/CH_4	20-25	13-16	7-9
CO/CO_2	40-60	2-3	1.5-2.0

sions contribute, too. No reproducible effect of electron trapping voltage on energy loss rate was observed; the onset of bursts during the ion decays complicated these measurements.

12.1. Interpretation of the observed lifetime

Can the observed confinement time reasonably be accounted for as due to particle loss via the charge transfer (electron transfer) between the residual gas molecules and the deuterium ion in magma? Table 3 gives cross sections (in units of 10^{-19} cm^2) for D 's of energy 600, 700, and 800 keV, incident on various atomic species (data interpolated from ORNL-5206).

Taking into account the data on the relative abundances of the background gas from the residual gas analyzer, as well as the fact that most gases are not absorbed well in the chamber walls, the dominant species after D_2 might be H_2O , with partial pressures possibly as high as 3×10^{-10} Torr. This must be compared to estimated D_2 pressures of $5-10 \times 10^{-9}$ Torr.

The cross sections will make the H_2O charge transfer event rate higher, but because of the higher density of D_2 , the two rates might be comparable. Energy dependences in the range of interest are similar; hence, pending availability of analysis of gas composition, we may define an effective density:

$$n_0 = n(D_2^+) + 12.5n(H_2O) + \dots \quad (20)$$

For deuterons in the range of $400 \text{ keV} < T < 1 \text{ MeV}$, we have (adapted from ORNL-3760, cross-checked against ORNL-5206 data) the lifetime against charge transfer formula:

$$\frac{1}{\tau_{ct}} = n_0 \sigma_{ct} v_d \frac{1.6 \times 10^6 n}{T_d^{5.5} (1 + 200/T_d)^5}, \quad (21)$$

where T_d is in keV. The CEND spectrum in fig. 14 is well fitted with eq. (21). With a nominal $n_0 = 10^{-8}$ Torr (3.6×10^8 molecules/cm 3), energies $T_d = 625, 650, 675, 700$, and 725 keV yielded τ 's of 16.6, 19.6, 23.1, 27.1, and 31.7 s, respectively. These are, in fact, consistent with the measured times of 20-40 s for decay of rf spectra after turning off the beam.

The fact that the longest lifetimes and highest densities were obtained with the highest D_2^+ injection energy of 1.45 MeV (magma D^+ energy 0.725 MeV) is in accord with the strong energy dependence of τ_{ct} . Improved estimates are needed that would take into account energy degradation – a significant but not overwhelming effect due to the $T^{5.5}$ dependence of τ_{ct} .

13. Electron temperature

Channon [13] has estimated the ambipolar potential difference that could be present between magma plasma and end walls given less than complete neutralization, modeled by assuming a sheet of constant net charge density in an annulus at $z = 0$:

$$n(r) = \begin{cases} N_e/\pi(r_2^2 - r_1^2) & \text{for } r_1 \leq r \leq r_2, \\ 0 & \text{elsewhere,} \end{cases} \quad (22)$$

where N_e is total excess charge.

An image charge formulation gives potential difference, $e\Phi$, from wall (at ground) to $r = z = 0$ in the plasma. With $r_2 = R_p - r_1$, $d = 4$ cm, and $N = 3 \times 10^{11}$ (maximum observed thus far was $N = 7 \times 10^{11}$ ions), numerical evaluations with $R_p = 10$ cm yield $e\Phi$ as a function of r_1 :

$r_1:$	0	1	2	3 cm
$e\Phi:$	3318	3076	2886	2730 eV

(23)

Fixing $r_1 = 0$ and varying R_p gives

$R_p:$	4	6	8	10 cm
$e\Phi:$	14682	7997	4950	3318 eV

(24)

These numbers are in rough agreement with one estimate of rf grid capacitance (10 pf), and with crude calculations that ignore the image charges as being too distant from $r = z = 0$ to have significant effect. Further improvement requires more detailed knowledge of the distribution of net charge than is now available.

In considering the probable effect of a more detailed calculation, we may note that the chief defect of the present one is the assumption that excess charge is uniformly distributed within an annulus whereas we probably should expect $n_e(r)$ and $n_i(r)$ to have their largest absolute difference at small r . As the second table above indicates, concentrating excess charge at moderately small r tends to increase $e\Phi$ sharply.

A salient experimental observation has been that variation of the ambipolar potential difference by application of a few hundred volts on the rf pickup grids has a strong effect. This we take as an indication that $e\Phi < 1000$ eV, which is consistent with earlier predictions [19] of 500–1000 eV. We estimate

$$T_e = 0.4 \pm 0.3 \text{ keV.} \quad (25)$$

We conclude that actual excess charge is limited to $N < 3 \times 10^{10}$. In the best runs, this would mean neutralization of $> 90\%$.

14. Undetermined parameters

Five major experimental parameters – ion number, density, storage time, energy loss rates, and average ion energy – and their properties have been determined in the experiment. Three other important parameters have not been adequately measured, which makes complete analysis of the data impossible. (i) T_e is necessary for the understanding of ion energy loss rates, collective behavior, ion trapping rates, etc. No accurate method for the measurement of either transverse or longitudinal electron temperature was installed. Efforts to estimate T_e from simple theory have encountered severe difficulties; numerous factors enter, and simple models of scattering losses and friction yield results much at variance with experiment. The most we can say of T_e is to state its wide range, eq. (25). (ii) The residual gas analyzer should have had a charge multiplier installed so that measurements can be made at operating pres-

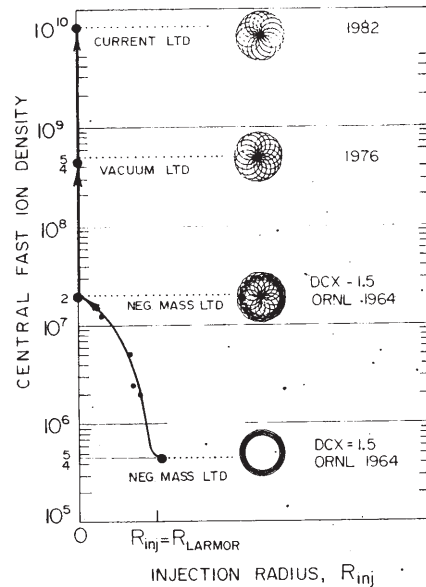


Fig. 17. History of negative mass instability: central fast ion density versus beam injection radial position. In DCX-1.5, the beam was injected peripherally (concentric orbits) and the negative mass instability prevented density increase above $4.5 \times 10^6 \text{ cm}^{-3}$. In one DCX-1.5 test, however, the density increased 40-fold when the injection was aimed at the center, but due to beam spread both the central orbits (magma) and concentric orbits were present. In the Migma III (1976) and Migma IV (1982) experiments, only the central orbits were formed and the central density increased $\sim 10^4$ times to $3 \times 10^{10} \text{ cm}^{-3}$.

limited to mean neu-

sures. (iii) Absence of position sensitivity in the charge exchange neutrals detectors has proven to be a serious hindrance.

15. Calibration of magnetic field with negative mass instability

The DCX experiments were plagued by the negative mass instability. In DCX-1, its threshold was $n_{\text{cfl}} = 5 \times 10^5 \text{ cm}^{-3}$; even for larger orbits, there were severe losses [2,3]. But in one run during the DCX-1.5 experiment, when the central (near-axis) injection was partially made, the instability threshold increased by a factor of 40 (fig. 17). With the pure central injection ($P_\theta \sim 0$), we find stability against negative mass up to the highest density reached, in agreement with both analytic calculations and simulations [20]. The negative mass instability was deliberately reproduced in our experiment in order to calibrate the magnetic field by steering the beam into concentric orbit, $b = r_L$, i.e., $P_\theta = \text{large}$. The instability was observed at a density four orders of magnitude below the maximum density used in this experiment, in agreement with earlier experiments. The instability and its associated ion signal behaved, in all respects, as expected. It seems clear that, under normal injection conditions, the negative mass instability will not pose problems for magma experiments.

16. Other instabilities

Previous experiments with small r_L observed flute instabilities at $n_v \sim 10^7 \text{ cm}^{-3}$. We observed no flute instability; this is consistent with DCX-1 experience and the trend of large-orbit measurements [6] in the Phoenix II device, which achieved $n_e = 2 \times 10^{10} \text{ cm}^{-3}$. However, the hot-ion component in Phoenix was only 15%, the remainder being the cold, ionized background gas. Even this density was reached only when stabilizing multipole fields were added; without them, the flute limited [21] the density to $3 \times 10^8 \text{ cm}^{-3}$. Hence, our results can be compared only with those of DCX-1. For the fusion consideration, we have also listed the TFTR parameters (table 4). The ion-cyclotron instability [22] was not seen.

17. Magma instabilities at reactor densities

While, technologically speaking, the experiment to reach reactor densities, $n \sim 10^{14} \text{ cm}^{-3}$, referred to as Magma V or DID (demonstration of ion densification), would be state-of-the-art, new and unexpected magma instabilities pose possible barriers to its achievement.

A theoretical problem with magma stability is the absence of stability theory for large gyroradius orbits.

Table 4
Comparison of the results of Magma IV experiment, DCX-1, and Tokamak TFTR

	Magma IV	DCX-1	TFTR
Ion species	d ⁺	p ⁺	p ⁺
Av. ion energy (keV)	700	300	10
Maximum central fast ion density			
$n_{\text{cfl}} (\text{cm}^{-3})$	$(3 \pm 2) \times 10^9$	2×10^8	
τ at maximum n_{cfl} (s)	20 ± 5	60	0.04
Negative mass instability threshold			
$n_{\text{cfl}} (\text{cm}^{-3})$	not observed	$(3-5) \times 10^5$	N/A
Number of stored ions N	$(3.2 \pm 5) \times 10^{11}$		N/A
Central density n_c (cm^{-3})	$(3 \pm 2) \times 10^{10}$		10^{14}
Triple product $Tn_c\tau$ (keV cm ⁻³ s)	4×10^{14}	2.5×10^{12}	2×10^{14}

With a few exceptions, all the plasma stability work done within the first three decades of fusion research was concerned with small Larmor radius orbit ("fluid") approximation, not valid for magma. Based on the plasma theories several types of instabilities should have occurred in the Magma III and IV experiments but none was observed (table 5). The major stability advantage of magma is its short axial extent, which follows from general principles and is valid even without detailed theory [23].

Recently, important progress was achieved in the theoretical understanding of stability for large ion Larmor radius plasmas. In a series of papers by the Los Alamos Group [24], using new computational techniques, stability results based on exact Vlasov kinetic theory are now available for theta pinches with and without field reversal. For the high- β rotating theta pinch ($\beta = 0.75$), the theory shows stability for $k_z M_0 > 0.02$, where $k_z = 2\pi/\lambda_z$ and M_0 = ion Larmor radius. A magma device will operate an order of magnitude above this threshold. Hence, it is applicable to the lithium magma where $R \sim 50M_0$. For the proton component of magma $R \sim 2r_0$, there has been no calculation for such a system.

The threshold result, however, has been obtained for a confinement system with radius R containing about $40 M_0$ and with a rigid rotor distribution function. Therefore, the result is only partially applicable to high density magma, although it looks encouraging. Work is in progress by Gratton and Ferro Fontan at the University of Buenos Aires (and presented at this symposium) to extend these results to a diamagnetic proton magma, using similar advanced theoretical methods for large orbits.

Table 5

Expected instabilities for Migma IV and IVb: Synopsis of stability tests ($\beta \ll 1$)

MIGMA IVa Medium density electrostatic regime	MIGMA IVb High density electrostatic regime
$B_0 = 3.3 \times 10^4$ G	Expected: $B_0 = 2.6 \times 10^4$ G, $I = 2$ mA
$\langle n \rangle_v = 3 \times 10^9$ cm $^{-3}$ (average)	$\langle n \rangle_v = 3 \times 10^{10}$ cm $^{-3}$
$n_c = 3 \times 10^{10}$ cm $^{-3}$ (center)	$n_c = 3 \times 10^{11}$ cm $^{-3}$
$\langle (\omega_{pi}/\omega_{ci})^2 \rangle = 0.3$	$\langle (\omega_{pi}/\omega_{ci})^2 \rangle = 3$
$(\omega_{pi}/\omega_{ci})_c^2 \sim 3$	$(\omega_{pi}/\omega_{ci})_c^2 = 30$
<i>Potential instabilities for this regime:</i>	
(None observed in Migma IVa)	
a) Negative mass	
b) Low frequency flute ($\omega_{pi}^2 \ll \omega_{ci}^2$) (medium density)	
c) Ion cyclotron resonant mode (medium density)	
d) Anisotropy in ion distribution Harris type; $T > T_{ }$	
e) Loss-cone, branch that couples electron waves with $n \omega_{ci}$	
<i>Main stabilizing features:</i>	
Large $R_{Li} = R_p/2$, $P_\theta \sim 0$ canonical momentum; small z length; metal walls in z; cold background;	
<i>Expected stabilizing effects:</i>	
$2R_{Li} = R_p$, $P_\theta = 0$; $E_i \neq 0$; higher T_e ; radial conducting walls; short length z; nonadiabatic z motions; z walls; precession and energy spread	

At this symposium, Berk, Rosenbluth, and Wong presented the first theory of magma stability [25]. Unfortunately, their theory is not applicable to time average neutralization; it assumes that magma is an electron Maxwellian gas. Note also the initial theoretical work of John Brandenburg (this symposium).

Two classes of external "corrective actions" for instabilities are possible in a magma because of its small volume and nonrandom motions of both ions and electrons: parametric stabilization and "dithering." Utilization of these techniques, which is not easily feasible in Maxwellian, large volume systems, is a salient part of the magma R&D program [26].

18. Migma as aneutronic power source: redirecting the program towards D³He reactor

This symposium has opened the way for a thrust towards a D + ³He magma reactor. Five independent papers from five labs in three countries show that the reactor's neutronicism is only 1–3%, i.e., ~100 times less neutronic than fission or conventional fusion; and that its radioactivity is 0.5%, i.e., ~200 times cleaner than fission or fusion. Our magma reactor simulations [27] show that D³He will ignite with a power output to input ratio $Q \sim 10^5$ and that its neutronicism $N = 3\%$ and radioactive content $R = 0.5\%$. Fig. 18 summarizes our conclusions on Q and N for D³He, ³He + ³He, and

³He + ⁶Li. The latter two show $Q \sim 1$ –2, i.e. a "driven" reactor, but no ignition. Perhaps based on these results, a National Research Council report [28] states that,

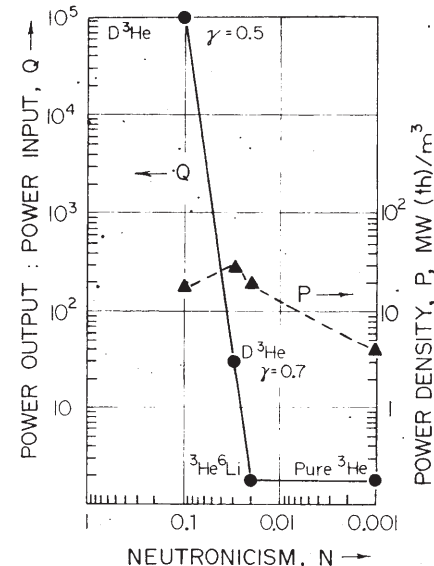


Fig. 18. Power gain Q and reactor power density P . P (MW(th)) as a function of neutronicism N , which is the fraction of total energy released carried by the neutrons, for reactors D³He ($\gamma = 0.5$), D³He ($\gamma = 0.7$), ³He-⁶Li, and pure ³He. γ is the ratio of D to ³He density. These are the results from the reactor simulation (ref. [27]).

wh

do

mc

apj

"n

sio

kir

ph

(se

of

abc

hav

the

tur

me

bes

Mi

wa

tio

and

nat

ach

18.

gra

nuc

ran

P_e

Fig.

while "the prospect for achieving aneutronic fusion is doubtful, the use of advanced fuels like D³He appears more feasible and offers many advantages for space applications" and that D³He is a "viable option" as "no other insurmountable technical problems are envisioned" after the improvement of plasma lifetimes, kinetic energy density, and mean energy. This emphasizes the importance of the Migma V experiment (see below).

The D³He reactor requires a mean ion temperature of 50–70 keV. Although this is an order of magnitude above that required for DT fusion, two ingenious ideas have been presented at the symposium, one by Coppi, the other by Momota, on how to reach such temperature in thermal plasmas using DT as an igniter.

Migma is thus far the only system that has experimentally demonstrated confinement of MeV ions; the best plasma machines have not exceeded 10 keV. Migma's factor of 100 advantage offers, in principle, a way to ignite nearly-aneutronic, nonradioactive reactions that require energies of between 70 keV (D³He) and 4 MeV (³He + ³He).

In view of these encouraging developments, it is natural that the magma program should be redirected to achieve an operating prototype of a D³He reactor.

18.1. Migma V experiment

The objective of our magma physics research program (fig. 19) is to demonstrate the feasibility of a nuclear power cell producing net electric power in the range

$$P_e = 1-2 \text{ MW(e)} \quad (26)$$

with an engineering power gain of the order of

$$G \geq 10^2. \quad (27)$$

This requires that the triple product of ion energy \times central density \times confinement time be increased from $\sim 10^{14}$ in Migma IV to

$$En\tau \sim 10^{16} \text{ keV cm}^{-3} \text{ s}. \quad (28)$$

This increase is the objective of the fifth and final stage of the program, the Migma V experiment. The fuel ion energy should decrease sevenfold, from 700 keV to

$$E_i \sim 100 \text{ keV}, \quad (29)$$

and the central fuel ion density should increase 3000-fold, from $3.2 \times 10^{10} \text{ cm}^{-3}$ to

$$n_c \simeq 10^{14} \text{ ions/cm}^3. \quad (30)$$

The confinement time of the fuel ions is expected to decrease by an order of magnitude with the density increase,

$$\tau = 3 \text{ s}. \quad (31)$$

Since objectives (29) and (31) have already been accomplished and exceeded in the Migma IV experiment, the research objective has been reduced to *increasing the fuel ion density* to value (30). This will be done by injecting accelerated beams of molecular ions of hydrogen, H₂⁺, to form the proton magma.

At the ion densities of the Migma V experiment, which are close to the reactor regime, the diamagnetic field of magma ions will *convert* the external maximum-*B* field into a minimum-*B* field [29]. In the center of such

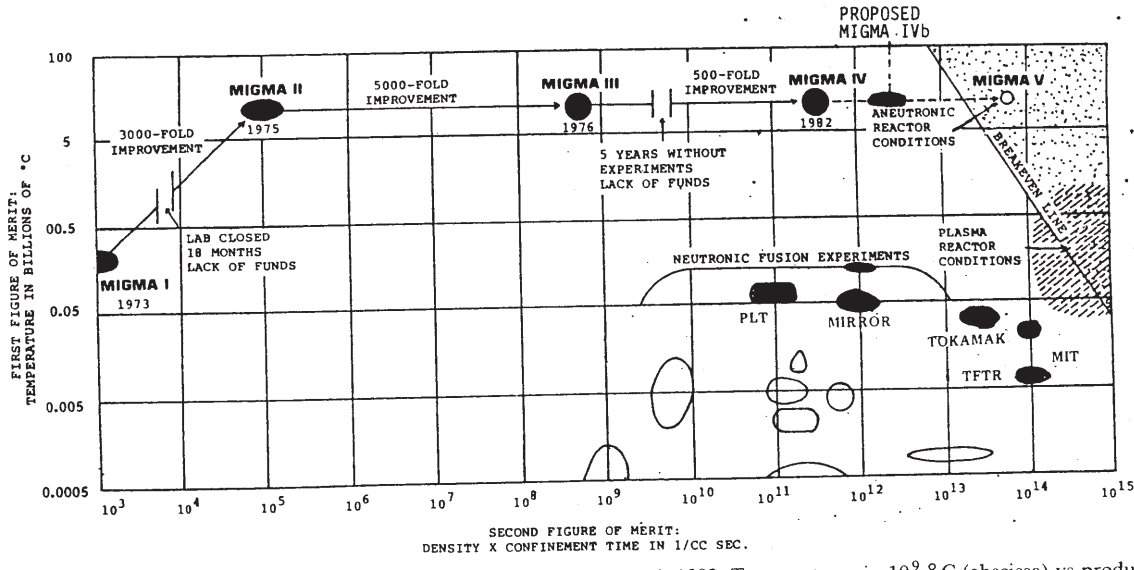


Fig. 19. Progress of magma experimentation (black dots) from 1973 through 1982. Temperatures in 10^9 °C (abscissa) vs product $n\tau$ ($\text{cm}^{-3} \text{ s}$). Neutronic fusion experiments are white areas.

a field, the local plasmic β can exceed unity (fig. 1c). The evolution from max- B to min- B is illustrated in fig. 3 of ref. [27] and fig. 2 of ref. [30]. We refer to this phenomenon as the diamagnetic surface magnetic confinement or "diasurmac." The effect is a consequence of the magma ion density being sharply peaked at the center. The diamagnetic field, whose sign is always opposite to that of the external fields, is similarly peaked in the center, thus it mostly cancels the field there.

The importance of diasurmac for advanced and aneutronic fuels is threefold: (1) it minimizes synchrotron radiation losses, which is especially important for aneutronic systems; (2) it establishes physical conditions known to provide MHD stability at high plasmic β values; and (3) it provides very high effective mirror ratios, of the order of 10^2 .

Intermediate experiment: A tenfold increase in n , to 10^{11} cm^{-3} , may be accomplished with an improved version of the present equipment (Magma IVb). Ref. [31] describes this experiment. For higher n , a new magnet and injector are required. They are within the state of the art.

19. Magma disc: maximal size of a "basic" magma power plant

Unlike other proposed fusion systems, the power of a basic magma plant cannot be scaled up. By "basic" magma, we mean a magma device using only one superconducting magnet consisting of a pair of coils plus a connecting pair. For $B = 10 \text{ T}$, the maximum size of the basic unit is limited to $1.5\text{--}3 \text{ MW(th)}$. Larger power units can be made by stacking in the same volume a large number of basic magma discs [32]. A disc's dimensions are determined by the energy of the protons from the $D + ^3\text{He}$ reaction and the requirement that they must be confined to provide ignition and the disc's thickness Z_0 by the requirement to control the time average neutralization of magma with external voltages, i.e., the disc must not be too thick. The intrinsic upper limit to the power output of the basic magma unit is the limit on the size of the magma volume V in eq. (1), which is determined by the gyroradius a in both the radius of magma, R , and its height Z_0 :

$$R = Ma, \quad (32)$$

$$Z_0 = A Ma, \quad (33)$$

where M is a multiplier and A the aspect ratio $A = Z_0/R$. For extremely diamagnetic magma, our studies show $M = 4$, and the stability considerations (electron oscillations through magma) $A \leq 1$. For the ring magnet [30,33] M may be perhaps as large as 5–6 but even this could be dangerous because it requires a large field-free region. Additional magnet loops at a smaller radius

might render it possible to have $M = 10\text{--}20$, but this would make magma a larger system approaching the complexity of the plasma machines, i.e., it would no longer be a basic magma. It is possible that once a basic magma module has been developed, any size power plant consisting of a large number of such modules might become so attractive from an engineering standpoint that the necessity for a complex, large power cell will no longer exist.

Our simulations of the type reported in ref. [27] show that an ignited $D^3\text{He}$ unit operating at a plasmic β of 0.98 will produce a net power P of $30 \text{ MW(th)}/\text{m}^3$ at 10 T . For a $D^3\text{He}$ magma-plasma disc of radius $R = 0.25 \text{ m}$, where $R = 4a$ and a is the radius of the proton from $D^3\text{He}$, the net power output will be

$$P = 0.15 B/A \text{ MW(th)}, \quad (34)$$

where B is the average external magnetic field (in tesla) and A the aspect ratio. For $B = 10 \text{ T}$ and $A = 1$, $P = 1.5 \text{ MW}$ per disc. Our design calls for 3–10 discs in the same volume. This is accomplished by axial stacking along the z axis. Assuming direct conversion with an efficiency of $3/4$, the basic magma electric power output is

$$P_e = 0.1125 B/A \text{ MW(e)}, \quad (35)$$

which, for $B = 10$, $A = 1$, gives $P = 1.125 \text{ MW(e)}$.

Our conceptual design of magma power plant assumes a conversion efficiency of 0.5, so that the 2 MW(e) plant will be a triplet of basic migmas in a single volume generating $4.5 \text{ MW(th)} = 2.2 \text{ MW(e)}$.

19.1. Basic magma power cell geometry

A small 2 MW(e) aneutronic power reactor will be a cylinder 1 m in diameter and 1.5 m long, containing 3 magma discs. The geometry of a magma aneutronic reactor [26] consisting of 3 to 10 discs is shown in fig. 20. Present estimates show that such a power source would yield anywhere between 30 kW(e) and 7 MW(e) of useable electric power. Such units could be mass-produced and power stations could then be made large or small.

19.2. Direct conversion

Even without direct conversion of nuclear energy released in magma into electricity, the aneutronic reactor gives useful power gain. Since in aneutronic reactions, almost all nuclear energy produced is carried by the charged particles as kinetic energy, it is possible to avoid the heat-steam generation cycle by direct conversion of the kinetic energy of the charged particles into electric energy. Studies of direct conversion for low energy ions (keV) at LLL have indicated conversion efficiencies of $> 80\%$.

, but this
iching the
would no
ice a basic
ize power
1 modules
ing stand-
power cell

n ref. [27]
a plasic
FW(th)/m³
of radius
radius of the
ll be

(34)

d (in tesla)
nd A = 1,
-10 discs in
ial stacking
on with an
ower output

(35)

W(e).
r plant as
that the 2
s in a single

or will be a
containing 3
aneutronic
own in fig.
ower source
nd 7 MW(e)
e mass-pro-
ade large or

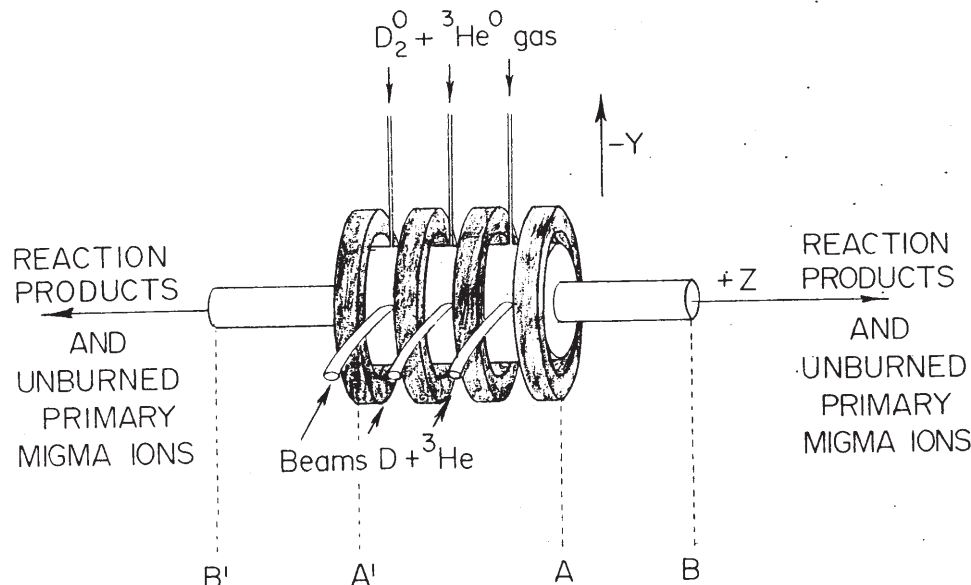


Fig. 20. Geometry of the triplet migma power cell. Three migma discs (not shown) are formed in the $x-y$ plane from the mixed $D^2 + ^3He^0$ gas. 10 s later, the beam injection is replaced by gas or pellet injection from the other side. $A'A$ = reaction chamber, AB = beam formation section. The beams consist of the nuclear reaction products, unused plasma ions and electrons formed and separated by placing a magnetic cusp at B and B' .

The conversion method for a migma reactor would differ essentially from other direct conversion schemes. As shown in figs. 8 and 9 of ref. [27], the ions exiting from the migmacell will not be thermalized, but will remain near their production energies (1–10 MeV). According to one of our concepts under consideration, the fusion products from a migmacell would be converted into two mixed ion-electron streams (one along

$+z$, the other along $-z$). The electrons will be separated from the ions by magnetic cusps at B and B' , then directed into two decelerators (fig. 21). The deceleration will result in the generation of high voltage in the range 100 kV–2 MV on the terminal of the decelerator. This voltage can be ac or dc, depending on whether or not the ejected beam will be modulated. Two exits facilitate the ac output.

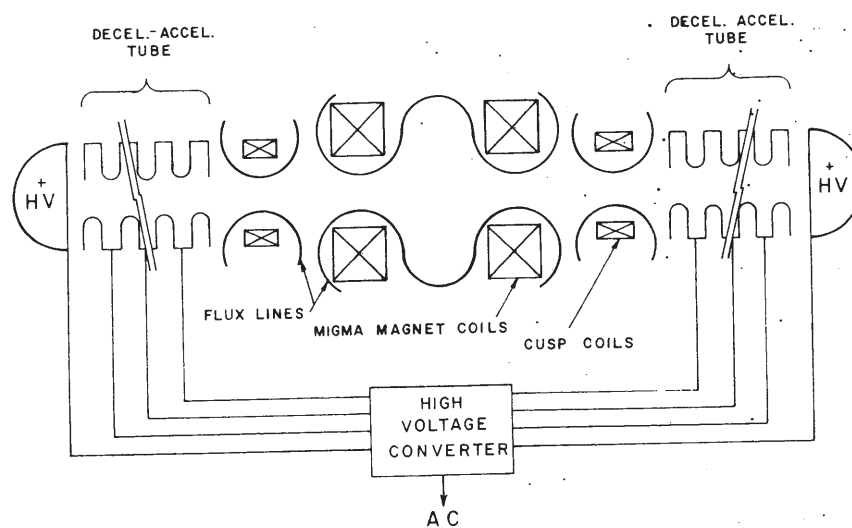


Fig. 21. Direct conversion by two decelerators. A migma disc is formed in the center and the two decelerators act as "plugs" and, at the same time, as convertors of the ions' kinetic energy into displacement potential buildup by deceleration. The z axis is horizontal. The ion orbits remain nearly parallel to the z axis until brought to a halt.

20. Long term availability of ^3He fuel

Helium-3 is a natural, nonradioactive, easily separable isotope of helium. Its abundance on Earth is 10^{-6} that of ^4He , (^4He : 99.99987%, ^3He : 0.00013%). Its extraterrestrial abundance is an order of magnitude greater.

At present, large quantities of ^3He are available in the United States. As tritium decays into helium with a half-life of 12 yr, ^3He is extracted annually from the hydrogen weapons arsenal. As a result, ^3He is an order of magnitude less expensive than tritium (table 6).

Questions on the longterm availability of ^3He on the Earth have been raised and termed a main obstacle to a practical D^3He reactor. Miley has shown, however [34], that availability of ^3He is not a legitimate issue.

Any system that can burn ^3He can breed ^3He . ^3He is copiously produced in $\text{D} + \text{D}$ and $\text{p} + ^6\text{Li}$ reactions at or near 1 MeV. Before the advent of magma, ^3He breeding was rejected as an impossibility because such temperatures were unthinkable. The fact is that the deuteron energy of the Migma III and IV experiments was sufficiently high to produce ^3He . Remote ^3He breeding plants based on $\text{D} + \text{D}$ reactions were proposed by the utilities [35] as far back as 1977. The $\text{D} + \text{D}$ reaction is 33% neutronic. We believe the best ^3He breeder would be the $\text{p} + ^6\text{Li}$ reaction, which is 2% neutronic [27]. The realization that a thermonuclear reactor cannot reach the temperature required to breed ^3He , coupled to the dogmatic assumption that thermonuclear reactors are the only possibility, has perpetuated misconceptions about the unavailability of ^3He on Earth and proposals for its mining on the moon.

Table 6
Aneutronic and neutronic fusion fuel costs^{a,b)}

Fuel	Supplier	Purity [%]	Cost [\$/k]	Unit fuel cost (FBU = 1.0) [mil/kW(th) h]
Fusion D	S.R.L.	99.1	1.06×10^3	0.0008
Fusion T	M.L.	> 94	7.5×10^6	42
Fusion ^3He	M.L.	99.9	7.35×10^5	4.5
Light fission ^6Li	O.R.N.L.	95	1.25×10^3	0.03
Light fission ^{11}B	E.P.	97	3.6×10^4	1.7
Heavy fission ^{238}U				47

^{a)} DOE established prices provided by J. Ratledge, C. Benson (ORNL).

^{b)} Prices and purities subject to revision based on demand and technological improvements.

21. Cost of fuel

Table 4 shows that the present aneutronic ^6Li fuel cost per kWh(th) is 1500 times lower than that of uranium fission (nonbreeder) fuel. The only fuel less expensive than ^6Li is deuterium.

In all DOE projections of DT fusion power, the cost of tritium is assumed to drop to "zero." Such a sharp drop in price of tritium production (from the present \$7 million/kg) has been examined and found not to be justified, because the highest contribution to tritium cost is the processing cost [36]. Comparison of all costs of high sulfur coal, fission, DT fusion, and aneutronic fission is given in table 4.

22. Plant capital cost (table 7)

a) 30 kW(e) plant: There is a great global demand for remote 30 kW(e) plants for telecommunication and radar stations. Our reactor studies [27] show a D^3He reactor thermal power density of $30 \text{ MW/m}^3 = 30 \text{ kW(th)/liter}$. This, with a conversion efficiency of 0.5, implies that a 2 liter magma disc would produce

$$\text{Reactor power} = 60 \text{ kW(th)} \approx 30 \text{ kW(e).} \quad (36)$$

This is close to the magma volume of the Migma V experiment (1 liter).

b) Small plant: 2 MW(e): While the fusion PWR and the fusion DT reactor would be economically unthinkable operating at any power level below 1000 MW(e), one 3-disc migmacell of a total of $0.133 \text{ m}^3 = 133 \text{ liters}$ or 45 liters/disc would yield a 2 MW(e) reactor.

c) Intermediate plant: 10 MW(e): Such a plant would consist of 10 migmacells of 10 discs each. As seen in table 5, the aneutronic power plant capital (installation) cost is *at least 5 times lower than PWR* and *almost 20*

Table 7
Capital cost per kW(e) installed capacity

Reactor type	Dollars per kW(e) for plant of size:		
	1 MW plant	100 MW plant	1200 MW
Fission (PWR)	7000	4000	2000
DT Fusion Tokamak	not feasible	10000	5000
Aneutronic MIGMA			
$^3\text{He} + ^3\text{He}$ fusion	1260 ^{a)}	720 ^{b)}	< 500 ^{c)}
$\text{p} + ^{11}\text{B}$ fission	1000 ^{a)}	570 ^{b)}	< 400 ^{c)}
$\text{p} + ^6\text{Li}$	not completed	not completed	

^{a)} One power cell.

^{b)} 100 cells 1 MW each.

^{c)} Estimated by the author on the basis of economy of mass production.

\approx ${}^6\text{Li}$ fuel
that of
fuel less

, the cost
h a sharp
present \$7
not to be
o tritium
all costs
neutronic

mand for
tion and
a $D^3\text{He}$
 $/m^3 = 30$
cy of 0.5,
ce

(36)

Magma V

PWR and
unthinka-
1 MW(e),
133 liters
or.
int would
s seen in
stallation)
almost 20

of size:
1200
MW
2000
5000
 $< 500 \text{ e}^{\circ}$
 $< 400 \text{ e}^{\circ}$

iy of mass

times lower than the projected DT fusion reactor (tokamak).

d) Large plant: 1000 MW(e). Such a plant would consist of 100 10-disc migmacells. Projections of a 1000-MW magma plant indicate a capital cost of one-fourth that for fission and less than one-tenth of the estimates for DT fusion (tokamak). Similarly, the ${}^6\text{Li}$ fuel cost is two orders of magnitude less than that of uranium and tritium.

23. Advantages of aneutronic power

Advantages of having power stations consisting of tens of thousands of 3-MW(e) power units are:

- Economy of mass production.
- Standardization in power plant construction.
- No minimum economical size plan - 1-100 MW(e) plants are likely to be economical.
- Minimal waste heat due to direct conversion.
- Local power plants for large buildings or blocks of houses would make consumers independent of the major power grid.
- Local power plants for peak load would become possible.
- Costly power transmission can be reduced.
- Decentralized power will make the country less vulnerable to nuclear attack, sabotage, and regional blackouts.
- Construction time should be much shorter than for other central power sources; thus, capacity may be added to the system more specifically tailored to the demand for new power, thus cutting the cost of inflation and interest during construction and reducing the potential for unused capacity due to inaccurate long-range energy demand forecasts.
- Smaller power plants are ideally suited for small communities in developed countries and for less-developed countries, for whom large central stations are impractical.
- Aneutronic power plants cannot proliferate nuclear weapons and have no radioactivity safety problems; thus they can be mass distributed without nuclear safeguards.
- Since they require little or no shielding and consume little fuel, aneutronic plants could be made compact and light and be used for aerospace propulsion, as well as for trains, commercial ships, and seacraft, or for space stations or other remote usage.

Acknowledgements

Thanks are due to my associates S. Menasian, J. Nering, R.A. Miller, D. Al-Salameh, B.R. Cheo, R. Leverton, C.Y. Wu, and S. Channon for discussion and

input to this review, and to J. Norwood Jr. and A. Newman for their valuable editorial suggestions on the paper.

References

- [1] D. Al-Salameh et al., Phys. Rev. Lett. 54 (1985) 796.
- [2] H. Postma et al., Phys. Rev. Lett. 16 (1966) 265.
- [3] J.L. Dunlap et al., Phys. Fluids 9 (1966) 199.
- [4] M.N. Rosenbluth et al., Nucl. Fusion Suppl. Pt. 1 (1962) 143.
- [5] A.B. Mikhailovskii, Instabilities of an Inhomogeneous Plasma, Theory of Plasma Instabilities, Vol 2 (Plenum, New York, 1974) p. 125.
- [6] L.G. Kuo et al., Phys. Fluids 7 (1964) 988.
- [7] W. Bernstein et al., in Proc. 2nd Int. Conf. on Plasma Physics and Controlled Nuclear Fusion Research, Culham, England (1965) (IAEA, Vienna, Austria, 1966) p. 23.
- [8] F. Gratton, Atomkernenergie 32 (1978) 121.
- [9] B. Maglich et al., Nucl. Instr. and Meth. 120 (1974) 309.
- [10] R. Macek and B. Maglich, Part. Accel. 1 (1970) 121.
- [11] B. Maglich et al., Phys. Rev. Lett. 27 (1971) 909; Appl. Phys. Lett. 26 (1975) 609.
- [12] R.A. Miller, Phys. Rev. Lett. 29 (1972) 1590.
- [13] Semi-annual Progress Report of Aneutronic Energy Laboratories (December 1982) ed., S. Menasian.
- [14] S. Channon et al., Split pair superconducting magnet system for self-colliding beam experiments, United Sciences report FEC-41-75 (1975).
- [15] S.C. Menasian et al., Nucl. Instr. and Meth. 144 (1977) 49.
- [16] J. Ferrer et al., Nucl. Instr. and Meth. 157 (1978) 269. For n distributions see fig. 9.
- [17] J. Ferrer et al., Nucl. Instr. and Meth. 144 (1977) 51.
- [18] B. Maglich, Principle of time average neutralization of fully ionized matter (United Sciences report FESS-73-20 (1973).
- [19] S. Channon and F. Gratton, United Sciences report FEC-3-78 (1978).
- [20] M. Emery and R.A. Miller, these Proceedings (Int. Symp. on Feasibility of Aneutronic Power, Princeton, NJ, 1988) Nucl. Instr. and Meth. A271 (1988) 134.
- [21] J.G. Cordey et al., in Proc. 3rd Int. Conf. on Plasma Physics and Controlled Nuclear Fusion Research, Novosibirsk, USSR (1968) (IAEA, Vienna, Austria, 1969).
- [22] L.G. Kuo et al., Phys. Fluids 7 (1964) 988.
- [23] Liu Chen, these Proceedings, p. 151.
- [24] C.E. Seyler, Phys. Fluids 22 (1979) 2324.
- [25] H. Berk, M. Rosenbluth, and H.V. Wong, these Proceedings, p. 107.
- [26] B. Maglich, Atomkernenergie 32 (1978) 100, in English.
- [27] C. Powell et al., these Proceedings, p. 108.
- [28] Air Force Studies Board Comm. on Advanced Fusion Power (report available from Air Force Studies Board; National Research Council, 2101 Constitution Avenue, NW, Washington DC 20814, USA National Academy Press, 1957).
- [29] S.R. Channon, J. Golden, and R.A. Miller, Phys. Rev. A17 (1978) 407.
- [30] B. Maglich, these Proceedings, p. 167.

- [31] J. Nering et al., these Proceedings, p. 155.
- [32] B. Maglich, Nucl. Instr. and Meth. 111 (1973) 213; Nucl. Instr. and Meth. 120 (1974) 309.
- [33] J. Blewett, these Proceedings, p. 214.
- [34] G. Miley, these Proceedings, p. 214.
- [35] C.P. Ashworth (Pacific Gas and Electric Co.) A user's

perspective on fusion, Part II, Annual Meeting AAAS, Denver (1977).

- [36] B. Maglich, Economic, engineering, and environmental problems with DT fusion, United Sciences report UNS-82-40 (1982).

SYN

S. T.

P.O.

The
on the
behav
discus
compa
partic

A
radiat
appro

$$\frac{dE}{dt} =$$

where
becon
from
with t
by ion
Nume

$$\frac{1}{E} \frac{dE}{dt}$$

(B, in
applic
electrc
Since
second
vanced
for co

For
an abs
emissi
tion w

emiss
absorp

as long
distribu
tu

$$\lambda_0 = ($$

we see
ciable
loss is

0168-90
(North-